Alteration Heterogeneities in Peridotites Exhumed on the Southern Wall of the Atlantis Massif (IODP Expedition 357)

Originally published in:
Journal of Petrology 59(7), https://doi.org/10.1093/petrology/egy065

Funding acknowledgement:
200021_156011 - Hierarchical carbon-fiber composites with tailored interphase obtained via electrophoretic deposition of magnetized and funtionalized carbon nanotubes (SNF)
163187 - Hydration and carbonation of mantle peridotite: Drilling the Atlantis Massif (MAR 30°N) and the Samail ophiolite (Oman) (SNF)

JOURNAL OF PETROLOGY

Journal of Petrology, 2018, Vol. 59, No. 7, 1329–1358
doi: 10.1093/petrology/egy065
Advance Access Publication Date: 22 June 2018
Original Article

OXFORD

Alteration Heterogeneities in Peridotites Exhumed on the Southern Wall of the Atlantis Massif (IODP Expedition 357)

Stéphane Rouméjon[1]*, Gretchen L. Früh-Green[1], Beth N. Orcutt[2] and the IODP Expedition 357 Science Party[†]

[1]Institute of Geochemistry and Petrology, ETH Zürich, CH-8092 Zürich, Switzerland and [2]Bigelow Laboratory for Ocean Sciences, East Boothbay, ME 04544, USA

*Corresponding author. E-mail: stephane.roumejon@erdw.ethz.ch
[†]http://publications.iodp.org/proceedings/357/357title.html#pgfId-632268.

Received October 20, 2017; Accepted June 11, 2018

ABSTRACT

Serpentinized and metasomatized peridotites intruded by gabbros and dolerites have been drilled on the southern wall of the Atlantis Massif (Mid-Atlantic Ridge, 30°N) during International Ocean Discovery Program (IODP) Expedition 357. They occur in seven holes from five sites making up an east–west-trending, spreading-parallel profile that crosscuts this exhumed detachment footwall. Here we have taken advantage of this sampling to study heterogeneities of alteration at scales less than a kilometer. We combine textural and mineralogical observations made on 77 samples with *in situ* major and trace element analyses in primary and serpentine minerals to provide a conceptual model for the development of alteration heterogeneities at the Atlantis Massif. Textural sequences and mineralogical assemblages reveal a transition between an initial pervasive phase of serpentinization and subsequent serpentinization and metasomatism focused along localized pathways preferentially used by hydrothermal fluids. We propose that these localized pathways are interconnected and form 100 m- to 1 km-sized cells in the detachment footwall. This change in fluid pathway distribution is accompanied by variable trace element enrichments in the serpentine textures: deep, syn-serpentinization fluid–peridotite interactions are considered the source of Cu, As, and Sb enrichments, whereas U and Sr enrichments are interpreted as markers of later, shallower fluid–serpentinized peridotite interaction. Alteration of gabbros and dolerites emplaced in the peridotite at different lithospheric levels leads to the development of amphibole-, chlorite- and/or talc-bearing textures as well as enrichments in light rare earth elements, Nb, Y, Th, and Ta in the serpentine textures of the surrounding peridotites. Combining these observations, we propose a model that places the drill holes in a conceptual frame involving mafic intrusions in the peridotites and heterogeneities during progressive alteration and emplacement on the seafloor.

Key words: Atlantis Massif; fluid–rock interaction; International Ocean Discovery Program (IODP); serpentinization

INTRODUCTION

Serpentinized and metasomatized peridotites intruded by mafic rocks are commonly exposed along slow- and ultraslow-spreading ridges (Cannat, 1993; Michael *et al.*, 2003; Sauter *et al.*, 2013) and crop out on the seafloor at the Atlantis Massif (Mid-Atlantic Ridge, MAR, 30°N; e.g. Blackman *et al.*, 2002; Karson *et al.*, 2006). These rocks are tectonically exhumed along large offset normal fault zones, known as detachment faults (Cann *et al.*, 1997; Blackman *et al.*, 1998), which extend from the base of the brittle lithosphere towards shallower domains where hydrothermal alteration is active. The detachment has a concave-downward shape (deMartin *et al.*, 2007) owing to its flexural rotation during

exhumation (Morris *et al.*, 2009) and crops out at low angle on the seafloor (Blackman *et al.*, 1998).

Altered upper mantle rocks, exposed on the ocean floor and in ophiolites, constitute highly reactive chemical and thermal systems, in which interaction with water to produce serpentinites has major consequences. Serpentinization affects the lithosphere physical properties (e.g. Escartín *et al.*, 1997; Miller & Christensen, 1997; Oufi *et al.*, 2002; Falcon-Suarez *et al.*, 2017) and chemical exchange between the crust and the ocean by trapping and releasing many major and minor chemical elements and volatiles, with important consequences for long-term global geochemical fluxes and biogeochemical cycles (e.g. Früh-Green *et al.*, 2004; Paulick *et al.*, 2006; Deschamps *et al.*, 2013). In particular, serpentinization reactions lead to the production of highly reduced fluids and result in high concentrations of H_2 and reduced C-species, including methane, ethane, propane, and straight-chain hydrocarbons (Proskurowski *et al.*, 2006, 2008; Konn *et al.*, 2009). These reduced species are believed to form through Fischer–Tropsch type reactions, catalyzed by Fe-, Ni-, and Cr-bearing minerals, and have important consequences for biological activity on and within the seafloor and for global geochemical cycles (Kelley *et al.*, 2005; Brazelton *et al.*, 2006). Serpentinites are also an important reservoir for carbon in the form of carbonate minerals, as well as abiotically and biotically produced organic carbon, all of which can survive in ancient mantle domains for hundreds of millions of years. As an exothermic reaction, serpentinization may also contribute some heat to enhance hydrothermal circulation (Kelley *et al.*, 2001; Lowell & Rona, 2002; Früh-Green *et al.*, 2003).

Six active hydrothermal sites along the MAR (the high-temperature Rainbow, Logatchev, Ashadze and Nibelungen fields, and the lower temperature Lost City and Saldanha hydrothermal fields) are currently known to be hosted in mafic and ultramafic basement rocks, but more are likely to be found. Lost City on the southern wall of the Atlantis Massif is unlike all other known hydrothermal systems along the MAR. Hydrothermal activity is characterized by large carbonate–brucite structures venting high-pH (9–11), $<100^{\circ}$C, Ca-rich, metal-poor hydrothermal fluids with high concentrations of H_2, CH_4, organic acids, and low molecular weight hydrocarbons, resulting from serpentinization processes at depth (Kelley *et al.*, 2001, 2005; Früh-Green *et al.*, 2003; Ludwig *et al.*, 2006; Proskurowski *et al.*, 2006, 2008; Lang *et al.*, 2010).

Peridotites recovered in different detachment systems along slow- and ultraslow-spreading ridges are heterogeneously altered. Although a serpentine mesh texture commonly develops during olivine hydration (e.g. Francis, 1956; Rouméjon & Cannat, 2014), diverse overprinting features are observed: these include multiple serpentine vein generations in the drilled holes of Ocean Drilling Project (ODP) Leg 153 (Kane area, MAR 23°N; Andreani *et al.*, 2007), serpentine recrystallization and veins in dredge samples along the easternmost Southwest Indian Ridge (SWIR; Rouméjon *et al.*, 2015), and talc metasomatism at the Atlantis Massif and elsewhere along the MAR (Boschi *et al.*, 2006*b*). In addition, at 15°N along the MAR eight holes were drilled at five sites during ODP Leg 209 (Kelemen *et al.*, 2004). The mineralogical assemblages comprise serpentine and magnetite that variably coexist with talc, brucite, iowaite, pyrite and/or hematite (Bach *et al.*, 2004) depending on the holes, and these correlate with specific bulk-rock trace element enrichments (Paulick *et al.*, 2006). This variability has been attributed to differences in temperature (e.g. talc or tremolite development instead of serpentine after orthopyroxene), redox state (e.g. presence of magnetite versus hematite), presence of altered mafic intervals responsible for high Si activity (talc replacing serpentine textures), or intensity of fluid fluxes (presence or absence of brucite). These textural, mineralogical and chemical features variably affect peridotites from the same dredge, dive or drill site, implying that the footwall of detachments is heterogeneous and that specific alteration processes probably occur at scales less than 1 km.

Our study aims to characterize the heterogeneities of peridotite alteration and takes advantage of closely spaced, shallow holes drilled across the southern wall of the Atlantis Massif during International Ocean Discovery Program (IODP) Expedition 357 (October–December 2015, R.R.S. *James Cook*; Früh-Green *et al.*, 2017). Sampling benefits from exceptionally good recoveries, allowing precise description of the contacts between lithologies in the cores. Here we combine core observations with textural sequences and mineralogical assemblages identified at the thin-section scale and complement these with *in situ* major and trace element analyses of primary (olivine, pyroxenes) and serpentine minerals. This leads us to propose a conceptual model for the evolution of the alteration heterogeneities in the detachment footwall of the Atlantis Massif during its exhumation, which are controlled by the initial distribution of primary lithologies and the reorganization of fluid pathways. Our study is based on samples that were altered and exhumed at depth on-axis and are likely to record fluid–rock interaction conditions that differ from those associated with the present-day, off-axis hydrothermal activity at the Lost City hydrothermal field.

GEOLOGICAL SETTING

The Atlantis Massif is a 1·5–2 Ma (Blackman *et al.*, 1998; Grimes *et al.*, 2008), dome-shaped bathymetric high located on the western flank of the MAR axial valley and bordered on the south by the Atlantis Fracture Zone (Fig. 1). The corrugated central dome (Cann *et al.*, 1997) was drilled during IODP Expeditions 304 and 305 in 2004–2005 (Blackman *et al.*, 2006) and recovered a 1400 m thick suite of dominantly mafic rocks, ranging from olivine-rich troctolites to oxide gabbros. In contrast,

the non-corrugated southern wall of the massif is dominated by variably altered ultramafic sequences with intermittent mafic plutonic intrusions. Exposures on the southern face are interpreted as a cross-section of the detachment system. Dredges and dive samples correspond to ~70% altered peridotites and ~30% altered mafic rocks (Blackman *et al.*, 2002; Boschi *et al.*, 2006*a*; Karson *et al.*, 2006). Observations from outcrop to microscopic scales reveal successive stages of deformation that affected the peridotites and mafic rocks from the detachment footwall during exhumation (Schroeder & John, 2004; Karson *et al.*, 2006). Whereas early ductile deformation produced localized mylonitic shear zones through the massive peridotite in a 500 m thick domain below the fault zone, later semi-brittle and brittle deformation features are localized in the 90 m below the fault zone (Schroeder & John, 2004). Brittle deformation postdates the onset of hydration that produced highly to fully serpentinized peridotites that are locally overprinted by Si-(talc) metasomatism in the deformed layers of the detachment fault zone (Boschi *et al.*, 2006*a*). At the Atlantis Massif, serpentinization is thought to strongly influence hydrothermal processes at the Lost City hydrothermal field (Kelley *et al.*, 2001, 2005; Früh-Green *et al.*, 2003). This off-axis hydrothermal field lies on the southern wall and corresponds to an end-member hydrothermal system, with brucite–carbonate chimneys and relatively low-temperature (40–90°C), highly alkaline (pH 9–11) fluids (Kelley *et al.*, 2001, 2005). These fluids are thought to derive from interaction between seawater-derived hydrothermal fluids and peridotites. Thus, the Atlantis Massif provides an ideal natural laboratory in which to study tectono-magmatic and alteration processes in oceanic core complexes, as well as off-axis, serpentinite-hosted hydrothermal activity and carbonate precipitation.

CORE LOCATIONS AND SAMPLING

IODP Expedition 357 (October–December 2015, R.R.S. *James Cook*; Früh-Green *et al.*, 2017) drilled a series of 17 shallow holes (maximum 16·5 m below seafloor, mbsf) at nine sites across the Atlantis Massif (Fig. 1). Here we focus on the five sites that contain altered peridotites. These sites are spread across the southern wall of the massif making up an east–west, spreading-parallel profile. Site M0071 marks the western end of the profile, Site M0068 the eastern end, and Sites M0069, M0072 and M0076 are central sites, located north of the Lost City hydrothermal field. The four remaining sites include rubble blocks of variable lithologies and sedimentary breccia with volcanic clasts and carbonate sediments (Früh-Green *et al.*, 2017). A short core of foraminiferous carbonate ooze was recovered at Site M0074 in the central dome, close to IODP Site U1309 where a total thickness of 1400 m of gabbroic plutonic rocks was recovered during Expedition 304/305 (Blackman *et al.*, 2006; Ildefonse *et al.*, 2007).

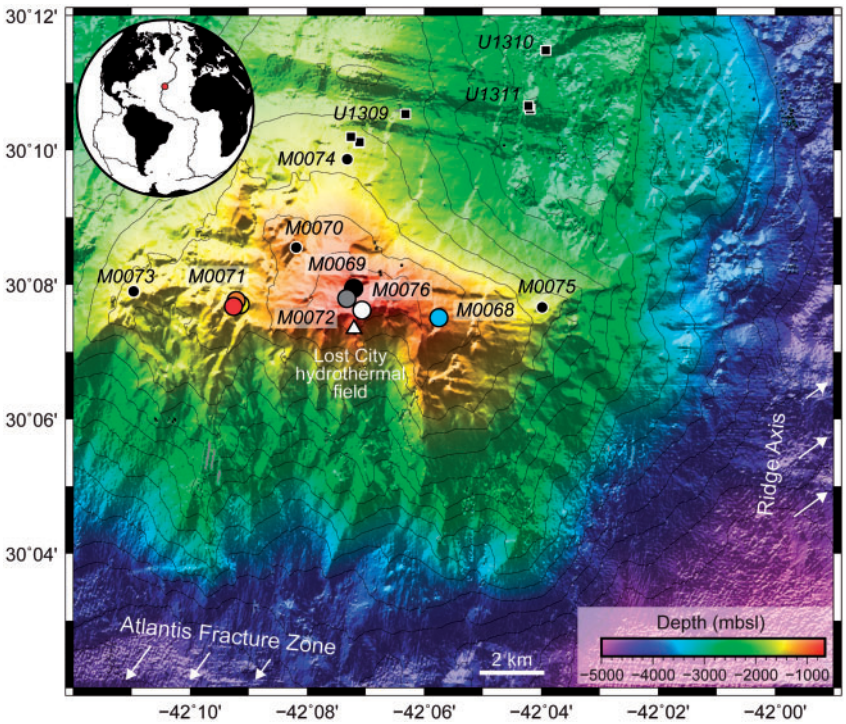

Fig. 1. Bathymetric map centered on the Atlantis Massif southern wall. The massif is located on the western flank of the Mid-Atlantic Ridge (MAR) axial valley (see inset) and bordered on the south by the Atlantis Fracture Zone. The colored dots correspond to the IODP Expedition 357 drill holes considered in this study. The small black circles mark other holes drilled during the expedition and the black squares are those drilled in the central dome during IODP Expedition 304/305. The position of the Lost City hydrothermal field is shown by the white triangle.

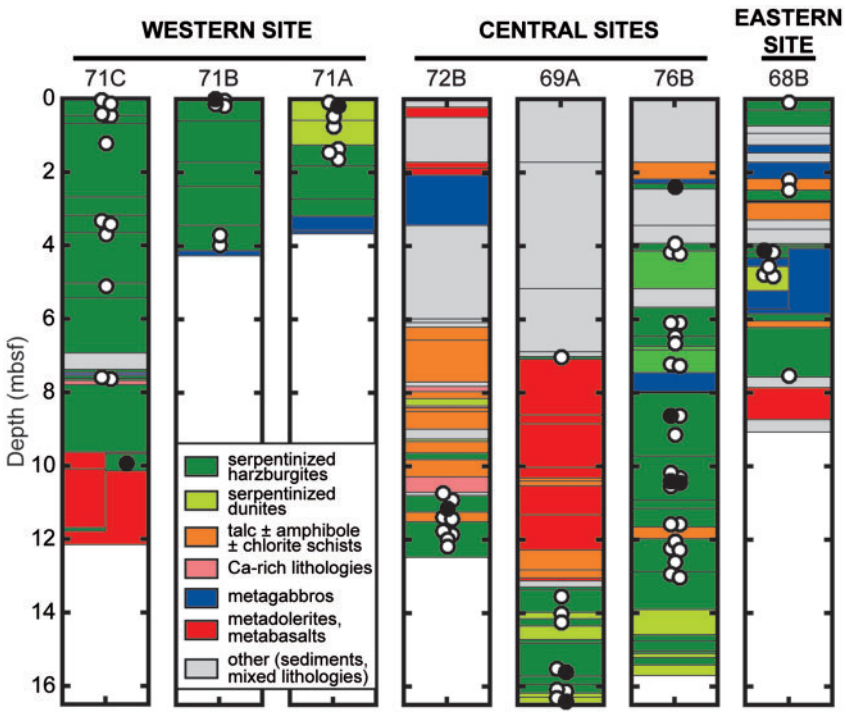

Fig. 2. Simplified logs of the dominant lithologies recovered in the seven holes containing serpentinized peridotites. The western and eastern holes exhibit rubbly intervals and sedimentary structures and are interpreted as products of mass wasting and local faulting, whereas the central holes represent *in situ* portions of the detachment footwall. The 66 white dots indicate samples used during our preliminary observations; the 11 black dots are the samples selected for further detailed investigations. Despite local dolerite intrusions, holes from Sites M0071 and M0069 are dominated by serpentinized harzburgites and dunites with very limited metagabbroic intervals. In contrast, Holes M0072B and M0068B contain more dolerites and gabbros, potentially Ca-rich metagabbros, and talc–amphibole–chlorite-bearing schists. Hole M0076B is intermediate, with a top portion containing metagabbros and talc–amphibole–chlorite-bearing schists, and a bottom portion dominated by serpentinized harzburgites and dunites.

The holes considered in this study benefit from remarkable recoveries for such settings, ranging between 30% (Hole M0071C) and 75% (Hole M0069A), with an overall recovery of 58%. Penetration depths ranged between 3·67 and 16·50 mbsf. Harzburgites and dunites dominate (44% by length), followed by metabasalts and metadolerites (24%), talc–amphibole–chlorite-bearing lithologies (11%), calcareous sediments (8%) and metagabbros (4%) (Früh-Green *et al.*, 2017). Figure 2 presents a simplified log of the various lithologies, with scans of typical cores recovered in these holes shown in Fig. 3.

Coherent, decimeter- to meter-long sections of cores, as well as structural measurements, indicate that the central sites are *in situ* portions of the Atlantis Massif basement (Früh-Green *et al.*, 2017). They record a complete history of processes affecting the peridotite-dominated domains of the lithosphere in the vicinity of the detachment fault zone during exhumation: early magmatic intrusions in the mantle, progressive serpentinization and metasomatism of these units, coeval dolerite intrusion at depth and superficial basaltic volcanism and final seafloor weathering. In contrast, the northwestern and most eastern sites contain rubbly intervals associated with well-preserved sedimentary structures pointing to a mass-wasting origin and local faulting. Although major structural relationships are lost at the northwestern and eastern sites, they still provide constraints on the tectonic, magmatic and alteration processes affecting the southern wall of the Atlantis Massif.

Microscopic observations were made on 77 thin sections distributed along these seven holes (dots in Fig. 2). Sampling covers the diversity of alteration textures in intervals with an inferred peridotite protolith. The protoliths correspond to 57 harzburgites and 20 dunites (Supplementary Data Table S1; supplementary data are available for downloading at http://www.petrology.oxfordjournals.org). Estimated modal proportions of primary minerals typically lie in the range of 60–100% for olivine, 0–40% for pyroxenes (including minor clinopyroxene), and $<$1–2% spinel. Sixty-four thin sections show complete replacement of olivine by serpentine, precluding characterization of mantle textures. Where olivine relicts are still present (13 thin sections), they generally do not exceed a few per cent of the rock and a few tens of microns in size. Fresh pyroxenes are rare (five occurrences out of 77 pseudomorphs analyzed in 11 samples) and are between a few hundreds of microns to several millimeters in size. Alteration of the pyroxenes is variable and led to serpentine (bastite texture), talc, tremolite, chlorite, or a mixture of these products. Spinels often show fresh cores with rims altered to iron oxides and sometimes

Fig. 3. Representative examples of typical peridotite-dominated cores in the selected holes. White continuous lines mark the contact between the peridotites and mafic intrusions. White dashed lines have been added to distinguish the background serpentinization from overprinting serpentinization textures and talc metasomatism. Figures 5a and 6c locations are indicated. Core M0071A-2R1 is composed of pervasively serpentinized harzburgites in contact with a gabbro altered to chlorite and amphibole. Core M0069A-10R3 is an example of a pervasively serpentinized dunite. Core M0076B-7R1 shows a pervasively serpentinized harzburgite overprinted by later serpentine textures (recrystallization and veins) and talc metasomatism. These overprints are localized in interconnected bands that surround mesh-textured cores. In Core M0072B-8R2, the pervasively serpentinized harzburgite is intruded by dolerites and overprinted by white (tremolite–chlorite) and grey (talc) domains. Core M0068B-2R1 shows talc metasomatism and pervasive propagation from a metagabbro inside the serpentinized harzburgite.

with a thin coating of chlorite (clinochlore). Thirty-three samples also show partial to complete replacement of serpentine by talc. In this case, the peridotite nature of the protolith was inferred from the presence of spinels

Table 1: Petrological description of the 11 serpentinized peridotites selected for detailed textural, mineralogical and geochemical analyses

Sample	Site	Hole	Core	Section	Interval (cm)		Depth (mbsf)		Protolith	Modal proportions (%)*			Primary mineral relicts	Mesh texture	Serpentine 2	Antigorite	Serpentine veins	Pyroxene alteration	Additional textures or phases
					top	bot.	top	bot.		ol	px	sp							
68B-1	68	B	4	1	14	17	4·14	4·17	harzburgite	70	30	<1	ol, px, sp	x	x	x	fibrous, gran–iso	serp, trem	
69A-4	69	A	10	1	91	95	15·63	15·67	harzburgite	80	20	1		x	x		fibrous	serp	
69A-6	69	A	10	3	10	12	16·39	16·41	dunite	100	0	1–2	sp	x			fibrous	—	
71A-1	71	A	1	1	21	24	0·21	0·24	dunite	100	0	2–3	sp	x			lam–isotr	—	carbonates
71B-3	71	B	1	cc	1	6	0·01	0·06	harzburgite	80	20	<1		x		x	fibrous, gran–iso	serp	
71C-5	71	C	9	1	24·5	26	9·92	9·93	harzburgite	80	20	<1	sp	x		x	fibrous	serp	
72B-1	72	B	8	1	43	45·5	11·14	11·16	harzburgite	70	30	<1	ol, sp	x	x		banded, gran–iso	serp, talc, trem, chl	mf-related domains
76B-1	76	B	2	1	66	69	2·38	2·41	harzburgite	80	20	<1	ol, sp	x	x	x	gran–iso	trem	mf-related domains
76B-6	76	B	6	1	65	68	8·63	8·66	harzburgite	70	30	0	ol	x	x		fibrous, banded	talc, trem	cpx vein
76B-7	76	B	7	1	68	71	10·40	10·43	harzburgite	90	10	<1			x	x	banded	serp, talc, trem, chl	
76B-8	76	B	7	1	74·5	77	10·47	10·49	harzburgite	80	20	<1		x	x	x	fibrous, banded	serp, talc	

*Visually estimated.
The petrological description of the 66 other samples is available in Supplementary Data Table S1. cc, core catcher; ol, olivine; px, pyroxene; sp, spinel; gran, granular; iso, isotropic; lam, lamellar; serp, serpentine; trem, tremolite; chl, chlorite; cpx, clinopyroxene; mf, microfracture.

or their ghosts. We selected a subset of 11 characteristic samples (Table 1) from the whole sample set to further characterize the sequences of serpentinization textures, the mineralogical assemblages, and the *in situ* chemistry of the serpentine minerals. These samples are represented in black in Fig. 2. For purposes of clarity, they have been given short sample numbers (refer to Table 1 for correspondence to the full IODP sample number).

ANALYTICAL METHODS

Thirty-μm-thick thin sections were used for Raman spectroscopy and electron microprobe analyses, and 80-μm-thick thin sections, produced on the same pieces of rock, were used for laser ablation inductively coupled plasma mass spectrometry (LA-ICP-MS) analyses. This allowed us to acquire a complete dataset on each texture or mineral targeted. Each of them was generally analyzed several times to ensure reliable and representative results. Only sample 69A-4 could not be analyzed with the LA-ICP-MS. All analyses were performed with facilities at the Department of Earth Sciences, ETH Zürich.

Micro-Raman spectroscopy

Micro-Raman spectroscopy allowed a quick identification of the minerals present. The system consisted of an Olympus BX40 microscope coupled with a Horiba LabRam spectrometer. We used a 532·1 nm solid-state laser with an emitting power of 500 mW. Using 10–20% of the power, a hole of 1200 μm, a slit of 200 μm, and a 100× objective led to an incident power of 5–12 mW and a spot size of <1 μm We generally ran three acquisitions of at least 5 s, with adjustments in case of insufficient quality of the spectra. We focused on the 100–1200 cm^{-1} and the 3650–3750 cm^{-1} ranges, with which all the phases present could be identified. In addition to the RRUFF database (http://rruff.info), we used previously published spectra (Rouméjon *et al.*, 2015, and references therein) to identify the dominant serpentine types. In this study, we interpreted serpentine spectra only as lizardite, chrysotile, antigorite, or possible mixtures between them. Polygonal serpentine could be present in some textures but does not yield a spectrum that is sufficiently different from those of chrysotile and chrysotile–lizardite mixtures to allow direct identification with micro-Raman (the same is true for polyhedral serpentine and lizardite). Examples of acquired spectra are presented in Supplementary Data Fig. S1.

Scanning electron microscopy and mineral chemistry

In addition to optical microscopy, we imaged details of thin sections using a JEOL JSM-6390 scanning electron microscope (SEM) operating at a voltage of 15 kV.

Major elements were acquired on a JEOL JXA-8200 electron microprobe, with a 15 kV acceleration voltage, a 10 nA beam current, and a 5 μm spot size. Each element was measured for 30 s (10 s for the background, 20 s for the peak) and standardization was made using natural and synthetic mineral standards. The targets were generally analyzed twice and the data averaged. Typical compositions are given in Table 2. The full dataset is available as Supplementary Data Table S2.

Thirty-five trace elements were measured using a Thermo Element XR ICP-MS system coupled with a Resonetics Resolution 155 LA system. The laser was fired with an energy density of 3·5 J cm^{-2}, a 193 nm wavelength, and a frequency of 5 Hz. Four pulses were shot during a few seconds with a spot size of 51 μm to clean the thin-section surface. After a 47 s blank, the target was ablated for 40 s with a 43 μm spot size. The time spent per element was 60 ms for rare earth elements (REE) and 20 ms for the rest. After every 25th analysis, the primary standard NIST612 was analyzed twice, and the two secondary standards GOR128-G (komatiite) and GSD-1G (synthetic glass with a basaltic composition in major elements) were analyzed once. This allowed us to estimate the precision on the data to be between 1 and 10% and the accuracy mostly between 5 and 30%. The data were then processed using the Matlab-based SILLS program (Guillong *et al.*, 2008) with silica and magnesium as internal standards. We finally discarded data too close to the detection limit [(value − 1σ error) $<$ detection limit] and values with errors higher than 75%. The targets were generally analyzed twice and the data were averaged. Typical compositions are given in Table 3. The full dataset is available as Supplementary Data Table S3.

RESULTS

Lithological variations

During IODP Expedition 357, seven holes at the five selected sites recovered serpentinized harzburgite with variable amounts of dunite. The lithologies and alteration in the three western holes (Holes M0071A, B, and C) and in the central Hole M0069A are relatively homogeneous and are dominated by serpentinized peridotites (Figs 2 and 3). At the western Site M0071, the serpentinized peridotites are crosscut by only minor intervals of gabbro altered to chlorite and amphibole. Hole M0071C contains additional thin and rubbly intervals of talc–amphibole–chlorite schists and Ca-rich metagabbros between 7 and 8 mbsf, and rubbly intervals of dolerites at the bottom of the hole. At Hole M0069A, in the central region, 7 m of sediments cover dolerites overlying serpentinized harzburgites and dunites. The contact between the serpentinized peridotites and the metadolerites is made up of an ∼15 cm thick interval of chlorite-dominated schist. At the bottom of the hole, the serpentinized peridotites host carbonate veins. Heterogeneity of lithology and alteration is greater in the central Holes M0072B and M0076B, and eastern Hole M0068B. These holes contain serpentinized peridotites alternating with higher amounts of

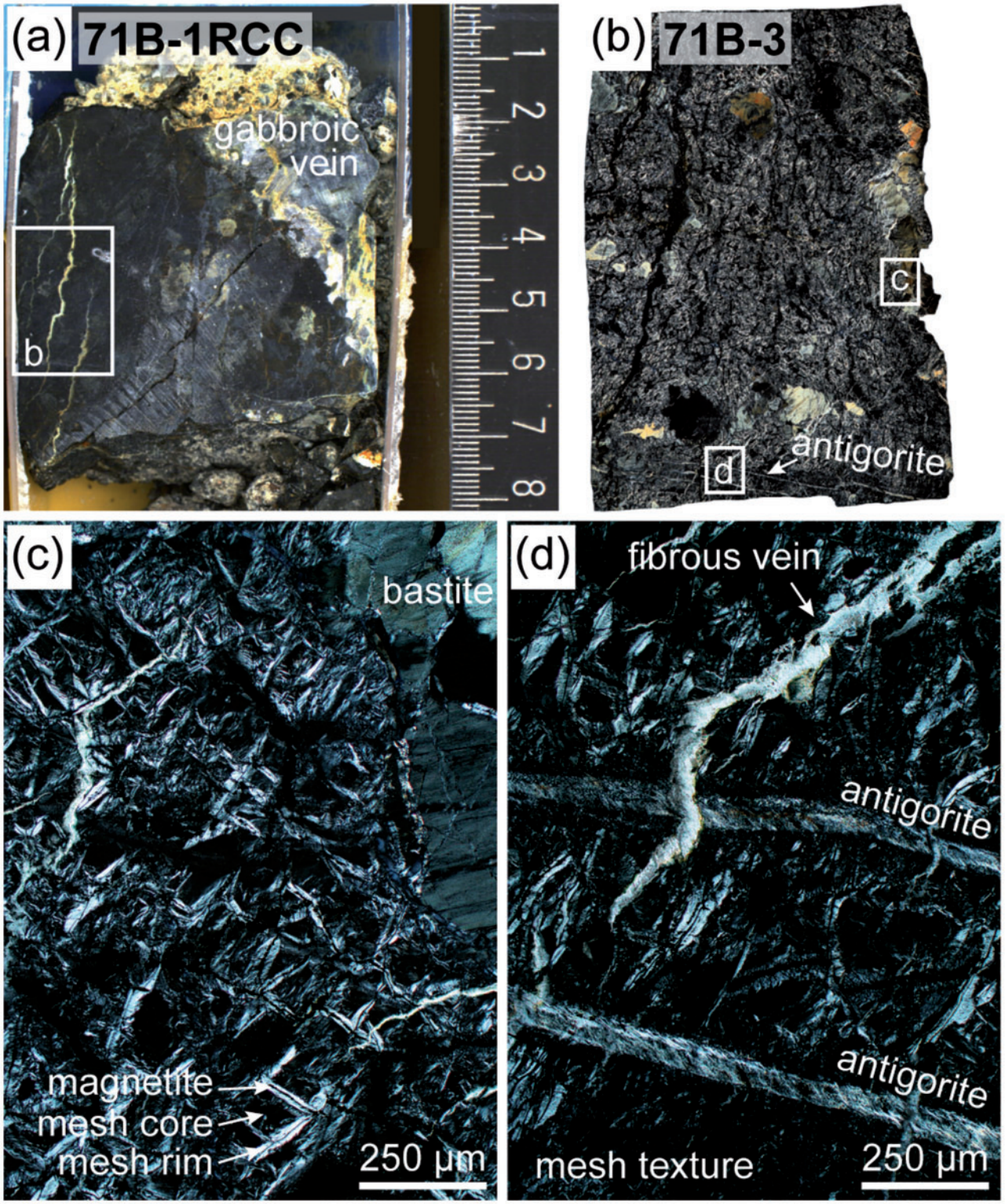

Fig. 4. Textural sequence at Site M0071, sharing similarities with Site M0069. (a) Scan of Core M0071B-1RCC (0–8 cm), a serpentinized harzburgite crosscut by a gabbroic vein (chlorite and amphibole) and serpentine veins. The gabbroic vein alteration did not affect the mineral assemblage of the surrounding serpentinization textures. (b) Scan of sample 71B-3 [location shown in (a)]: antigorite-bearing planes crosscut the mesh texture whereas orthopyroxenes are pseudomorphosed by bastite. (c) Photomicrograph of the mesh texture after olivine and bastite after orthopyroxenes. Each cell of the mesh texture comprises a mesh rim (lizardite) and a mesh core (lizardite and/or chrysotile). Magnetite concentrations are found in the mesh rims along the microfractures that initially crosscut the olivine. (d) Photomicrograph of the mesh texture crosscut by antigorite planes, which themselves are crosscut by extensive fibrous veins (chrysotile). The thin section scan and photomicrographs were taken under cross-polarized light.

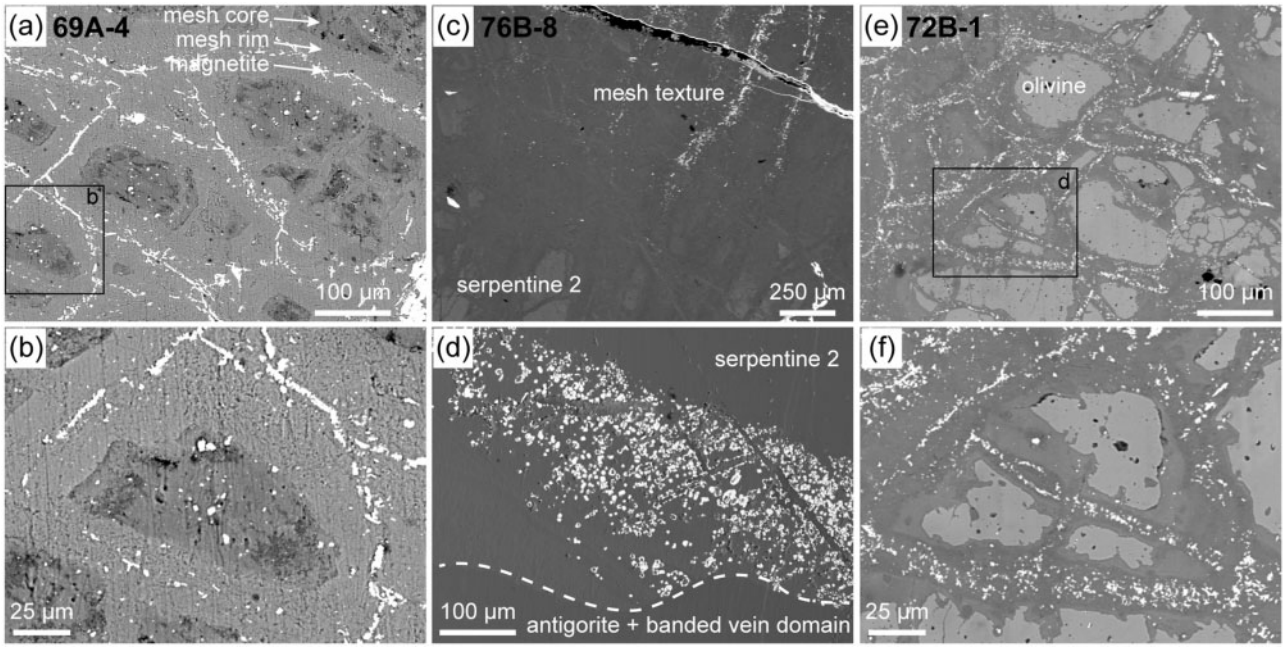

Fig. 5. Scanning electron microscopy (SEM) images of magnetite concentrations in serpentine textures. (a) Fully serpentinized mesh texture in sample 69A-4 in which serpentine mesh cores and mesh rims, and magnetite can be distinguished. (b) Close-up showing magnetite concentrated as a thin line along some microfractures between mesh rims. (c) Transition between the fully serpentinized mesh texture of sample 76B-8 and the magnetite-free serpentine 2 recrystallization texture. The transition between the two textures locally conserves a mesh-like texture although most of the lizardite is replaced by chrysotile. (d) One centimeter away, the magnetite corresponding to the serpentine 2 domain is concentrated along the edge of the antigorite-banded vein domain. (e) Partially serpentinized mesh texture in sample 72B-1 with visible olivine relicts in the mesh cores. (f) In comparison with (b), magnetite in mesh rims is more dispersed.

gabbro that are locally altered to Ca-rich intervals or talc–amphibole–chlorite schists. In Hole M0072B, mafic intrusions (gabbros and dolerites) are surrounded by white zones of an amphibole–chlorite assemblage coated by talc that overprints the serpentinized peridotites. Locally, this hole also contains light brown intervals of metagabbro associated with chlorite-rich intervals that are commonly described as blackwalls. In Hole M0076B, gabbroic intervals are altered and lead to 10–20 cm thick layers of chlorite blackwall and amphibole–chlorite assemblages. The serpentinized peridotites are affected by a localized talc metasomatism above 12 mbsf with talc-rich zones surrounding decimeter-sized serpentinized intervals of core. In core M0076B-7R1, talc develops within zones of rusty brown serpentine rims and veins that make up individual, oriented, 20–30 cm long lenses. Below 12 mbsf, mafic intervals are absent and late carbonate veins crosscut the serpentinized peridotites. In Hole M0068B, talc metasomatism progresses pervasively from the altered gabbros into the serpentinized peridotites.

Sequence of alteration textures and mineralogical assemblages

In the peridotites drilled at the Atlantis Massif during IODP Expedition 357, the sequence of alteration textures and the associated mineral assemblages vary between sites and sometimes downhole (Fig. 2). The sequences comprise successive serpentinization textures with local occurrences of amphibole–chlorite and/or talc-bearing textures.

Harzburgites and dunites from Sites M0069 and M0071 underwent pervasive and complete replacement of primary olivine and pyroxene by serpentine and magnetite. Gabbroic intrusions are scarce and are highly altered to chlorite and amphibole, but do not affect the mineral assemblage of the surrounding serpentinization textures (Fig. 4a and b). Olivine alteration has led to a typical serpentine mesh texture (Fig. 4c). Mesh cells are tens to hundreds of microns in size and are delimited by the microfractures that initially crosscut the olivine. Lizardite mesh rims form the outer part of a cell, whereas the mesh core, made up of poorly crystallized lizardite and/or chrysotile, constitutes its center. Magnetite crystallizes in the mesh rims and concentrates along microfractures (Fig. 5a and b). These magnetite concentrations are heterogeneous and are largest along microfractures associated with the largest mesh rims. Such texture is ubiquitous at the five sites. In parallel, orthopyroxenes are pseudomorphed by bastites (Fig. 4b and c) composed of lizardite and/or chrysotile, and occasionally antigorite. In addition, tremolite after orthopyroxene was found at Site M0069A. At Site M0071, antigorite overprints the mesh texture as bands of interpenetrating to interlocking textures that crosscut the whole thin section (Fig. 4b and d). Antigorite

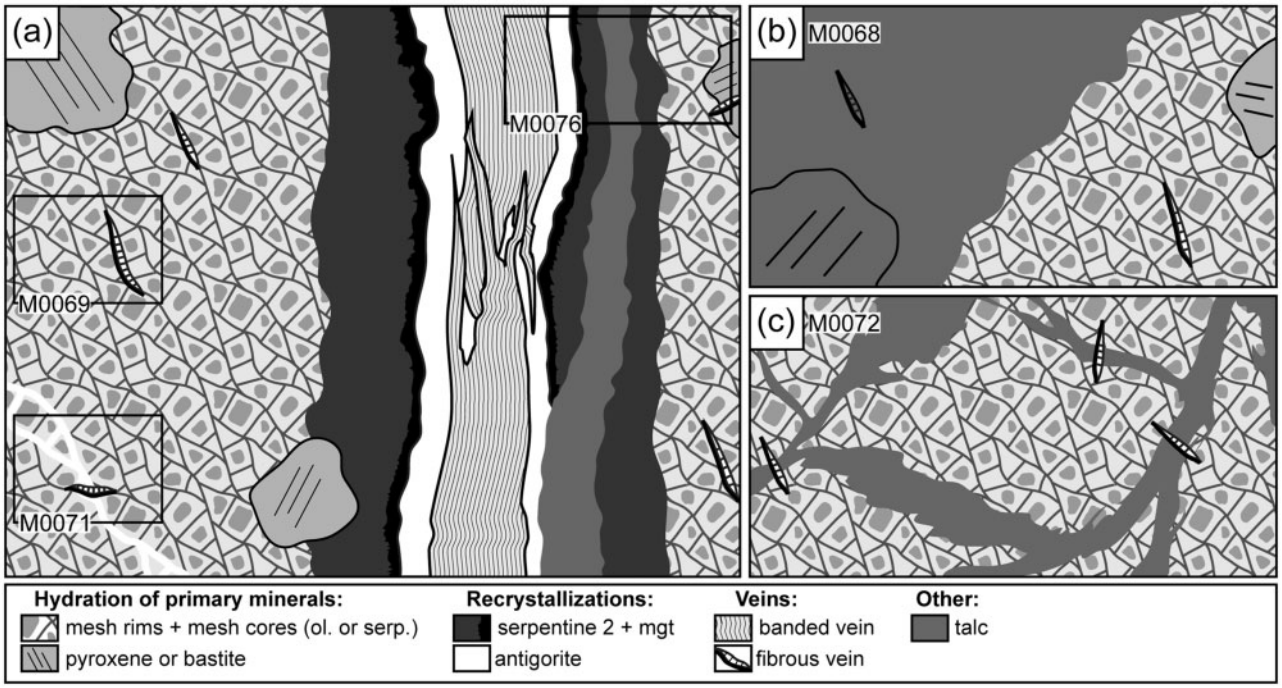

Fig. 6. Compilation sketch summarizing the textural sequences observed in peridotites at the different sites: (a) mesh texture overprinted by antigorite and/or fibrous veins (Sites M0069 and M0071; Fig. 4d), or by serpentine 2, antigorite and banded vein ± talc (Site M0076; Fig. 7b); (b) serpentine textures replaced by talc metasomatism (Site M0068; Fig. 8b); (c) mesh texture overprinted by the microfracture-related domains represented here filled with talc (Site M0072; Fig. 8d).

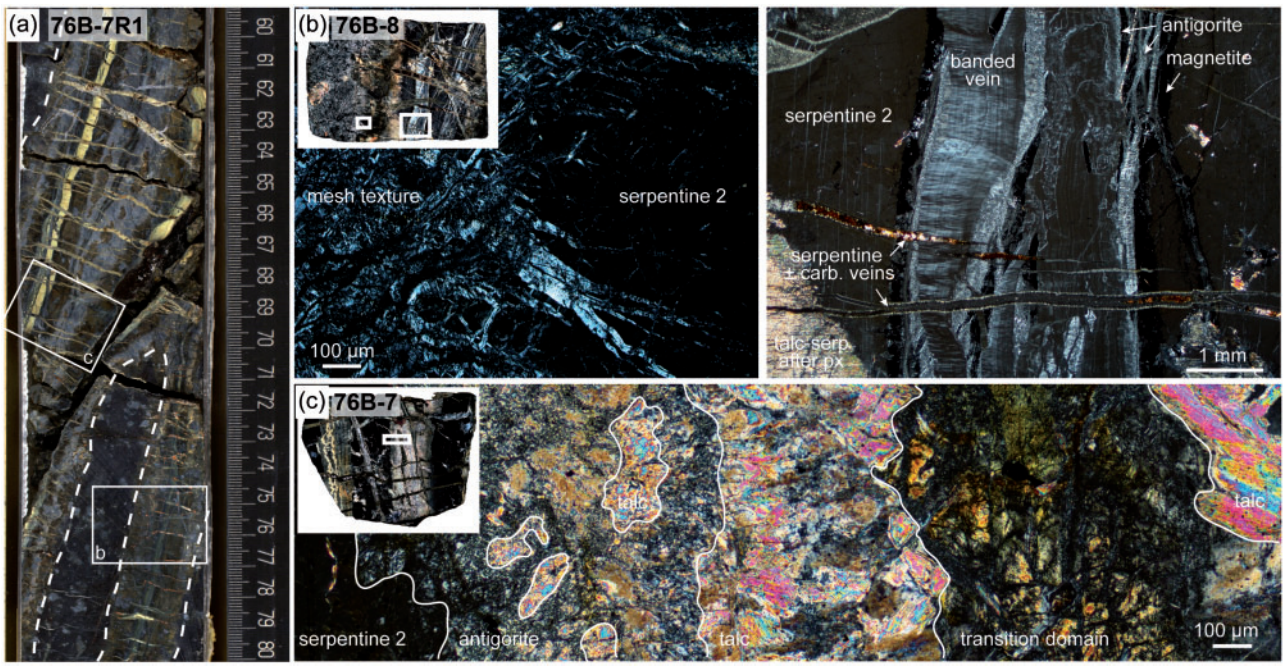

Fig. 7. Textural sequence in Hole M0076B. (a) Scan of Core M0076B-7R1 (60–80 cm), an initially pervasively serpentinized harzburgite in which mesh-textured domains are surrounded by rims of later serpentine textures and talc. (b) Sample 76B-8: the lizardite mesh texture is recrystallized into the chrysotile serpentine 2 (left photomicrograph). These recrystallized domains contain a central zone with antigorite and chrysotile ± polygonal serpentine banded veins, surrounded by magnetite concentrations (right photomicrograph). Pyroxenes are variably altered to talc, tremolite, chlorite and serpentine. Late, lens-shaped veins are filled with serpentine ± carbonate. (c) Sample 76B-7: in places, the serpentine 2 texture (background of the thin section) laterally shows a transition to talc via antigorite. Talc surrounds lens of mixed serpentine and talc (according to Raman spectroscopy) referred to as transition domains. In this talc-rich interval, late lens-shaped veins are filled by talc, locally rimmed by antigorite along the vein walls. The thin-section scans and photomicrographs were taken under cross-polarized light.

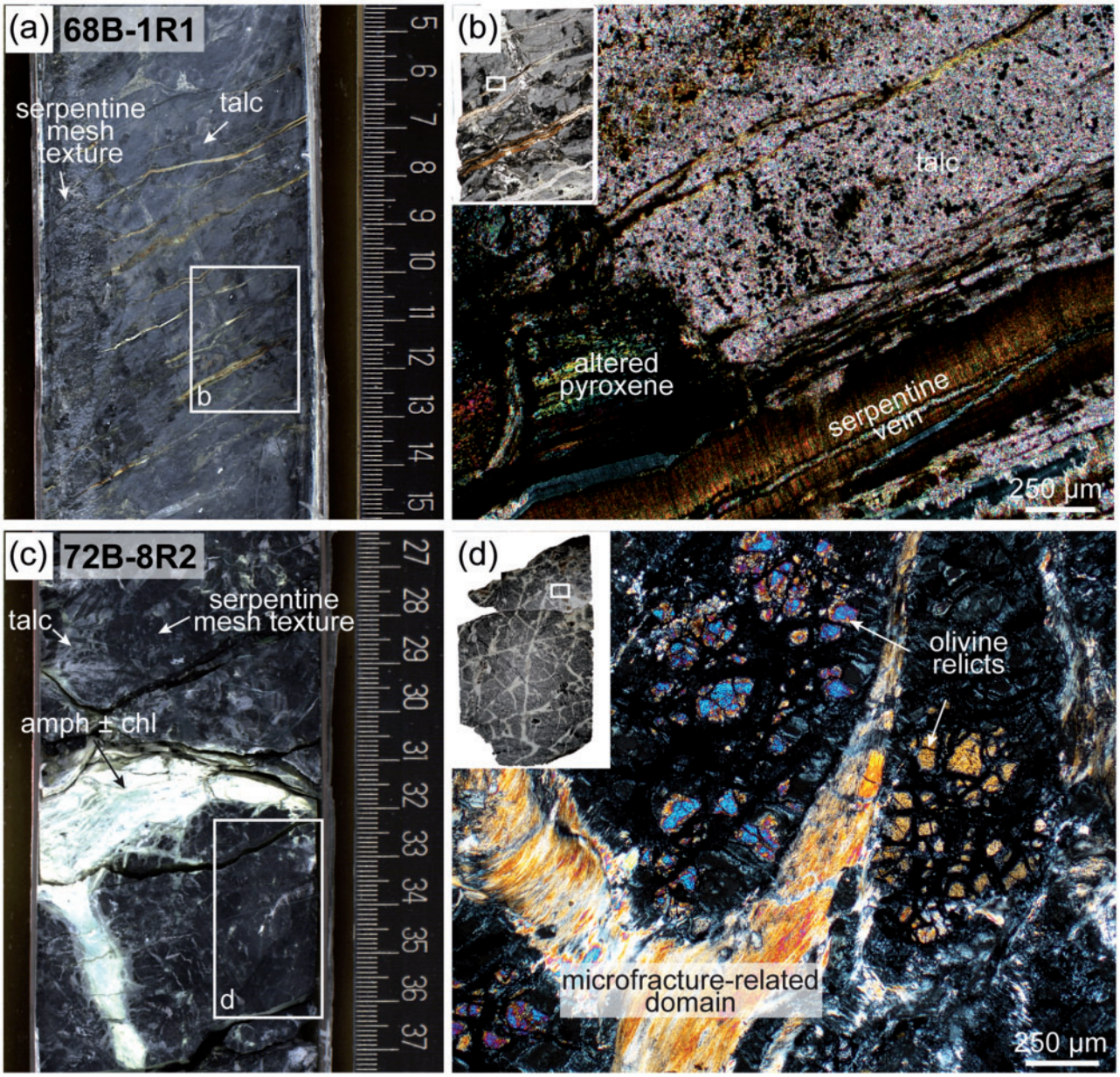

Fig. 8. Textural sequences in Holes M0068B and M0072B. (a) Scan of Core M0068B-1R1 (5–15 cm) in which talc metasomatism pervasively replaces the serpentine textures in harzburgites. (b) Photomicrograph of talc replacing the mesh texture and the altered pyroxenes. Magnetite appears to be conserved during the replacement. (c) Scan of Core M0072B-7R2 (27–37 cm) showing the pervasively serpentinized harzburgites crosscut by tremolite ± chlorite (in white) and talc (grey) domains. (d) Sample 72B-2: photomicrograph of these domains, referred to as microfracture-related domains, crosscutting the mesh texture in which olivine relicts are preserved. The thin-section scans and photomicrographs were taken under cross-polarized light.

develops along continuous microfractures in the mesh texture (Fig. 6a) and progresses inside the mesh rims, suggesting its growth after lizardite. Although it represents only a few per cent of the rock, antigorite crystallization is significant at Site M0071 and is observed in 14 out of 17 harzburgite samples selected from these holes. In contrast, it remains absent in the five dunite samples and in the Site M0069 cores. The last systematic stage of serpentinization at Sites M0069 and M0071 is the formation of extensive lens-shaped chrysotile veins, with chrysotile fibers parallel to the opening direction and joining the two walls of the vein (Figs 4d and 6a). They most often show one or two preferential orientations, parallel to the mesh texture microfractures and crosscuting the antigorite if present. Later serpentine veins (e.g. Fig. 4a, left side of the core) occasionally develop without preferential orientation and show variable texture or serpentine mineralogy.

Hole M0076B is the only example where the pervasive magnetite-bearing mesh texture is significantly overprinted by further localized serpentinization.

Table 2: Representative major element analyses (in wt %) for primary and serpentine minerals

Sample: Texture:	68B-1 olivine	76B-1 olivine	68B-1 enstatite	68B-1 enstatite	68B-1 bastite	69A-4 bastite	71C-5 bastite	71C-5 mesh rim	72B-1 mesh rim	76B-8 mesh rim	69A-4 mesh core	72B-1 mesh core	76B-6 mesh core
SiO_2	40·53	40·92	56·32	57·70	42·11	40·34	37·95	42·78	40·76	42·52	40·71	41·35	42·27
Na_2O	0·00	0·02	0·01	0·00	0·00	0·02	0·03	0·00	0·00	0·00	0·01	0·02	0·00
CaO	0·11	0·01	0·67	0·26	0·36	0·06	0·02	0·02	0·06	0·03	0·05	0·04	0·00
Cl	0·00	0·00	0·00	0·00	0·02	0·14	0·05	0·01	0·09	0·02	0·07	0·10	0·02
FeO	9·03	8·86	5·81	5·73	2·96	4·87	3·70	2·43	4·95	2·27	3·88	2·75	4·33
MgO	49·41	49·93	33·52	35·00	36·96	34·18	36·71	39·71	38·54	40·92	39·14	39·31	39·95
Cr_2O_3	0·03	0·02	0·58	0·19	0·57	0·94	0·95	0·05	0·00	0·02	0·03	0·00	0·00
K_2O	0·00	0·00	0·01	0·02	0·01	0·01	0·00	0·01	0·02	0·00	0·00	0·03	0·00
MnO	0·11	0·11	0·14	0·16	0·06	0·13	0·10	0·05	0·07	0·02	0·07	0·07	0·04
Al_2O_3	0·04	0·00	2·18	0·38	1·64	1·07	4·67	0·54	0·00	0·02	0·69	0·01	0·25
TiO_2	0·03	0·02	0·04	0·03	0·07	0·04	0·03	0·03	0·03	0·04	0·03	0·03	0·07
NiO	0·39	0·39	0·09	0·15	0·11	0·18	0·09	0·12	0·22	0·31	0·42	0·27	0·31
Total	99·69	100·28	99·36	99·61	84·86	81·97	84·29	85·75	84·74	86·18	85·10	83·98	87·23
Si	0·99	1·00	0·98	1·00	2·02	2·03	1·85	2·02	1·99	2·01	1·97	2·01	1·99
Na	0·00	0·00	0·00	0·00	0·00	0·00	0·00	0·00	0·00	0·00	0·00	0·00	0·00
Ca	0·00	0·00	0·01	0·00	0·02	0·00	0·00	0·00	0·00	0·00	0·00	0·00	0·00
Cl	0·00	0·00	0·00	0·00	0·00	0·01	0·00	0·00	0·01	0·00	0·01	0·01	0·00
Fe	0·19	0·18	0·08	0·08	0·12	0·20	0·15	0·10	0·20	0·09	0·16	0·11	0·17
Mg	1·81	1·81	0·87	0·90	2·64	2·56	2·67	2·80	2·80	2·88	2·82	2·85	2·81
Cr	0·00	0·00	0·01	0·00	0·02	0·04	0·04	0·00	0·00	0·00	0·00	0·00	0·00
K	0·00	0·00	0·00	0·00	0·00	0·00	0·00	0·00	0·00	0·00	0·00	0·00	0·00
Mn	0·00	0·00	0·00	0·00	0·00	0·01	0·00	0·00	0·00	0·00	0·00	0·00	0·00
Al	0·00	0·00	0·04	0·01	0·09	0·06	0·27	0·03	0·00	0·00	0·04	0·00	0·01
Ti	0·00	0·00	0·00	0·00	0·00	0·00	0·00	0·00	0·00	0·00	0·00	0·00	0·00
Ni	0·01	0·01	0·00	0·00	0·00	0·01	0·00	0·00	0·01	0·01	0·02	0·01	0·01
OH	0·00	0·00	0·00	0·00	4·00	3·99	4·00	4·00	3·99	4·00	3·99	3·99	4·00
Total	3·00	3·00	2·00	2·00	8·92	8·90	8·99	8·96	9·00	8·99	9·00	8·98	9·00
Total cations	3·00	3·00	2·00	2·00	4·92	4·92	4·99	4·96	5·01	4·99	5·01	4·99	5·00

(continued)

Around 9–11 mbsf, 10 cm sized mesh-textured domains are surrounded by centimeter-wide, rusty brown serpentine rims containing yellow continuous serpentine veins in the center and haloes of light grey talc (Figs 3 and 7a). At the microscopic scale, the mesh texture progressively vanishes in favor of the brown rims, which show a homogeneous and isotropic texture under cross-polarized light (Figs 6a and 7b, c; see also Fig. 5c). This recrystallization texture is referred to here as serpentine 2 and is primarily chrysotile (± lizardite) according to micro-Raman spectroscopy. This therefore marks the transition from a lizardite-dominated mesh texture to a chrysotile-dominated serpentine 2. Magnetite is absent in the serpentine 2 except at the contact with the central vein zone where it forms broad concentrations (Figs 5d and 7b). This zone contains elongated antigorite domains and millimeter-wide banded veins. Crosscutting relationships indicate that antigorite develops similarly to what is observed at Site M0071 and predates banded vein emplacement. The banded veins are made up of multiple ∼1-μm-thick bands of serpentine (chrysotile ± lizardite) oriented parallel to the vein wall. These veins develop as en echelon lens-shaped veins that ultimately join and produce the continuity observed in the cores. In Hole M0076B, orthopyroxenes are variably altered to serpentine, talc, tremolite or chlorite, whereas clinopyroxenes can be replaced by tremolite. In most cases, two or three of these phases coexist in the pyroxene pseudomorphs.

Subsequent talc metasomatism localizes in the serpentine 2 rims at Hole M0076B, away from the contact with the central vein zone (Fig. 7a and c). At the microscopic scale, talc is separated from the serpentine 2 by antigorite, and also surrounds lenses, visible on the core scan, that display an amber mesh-like texture under cross-polarized light. Such texture is unique to Hole M0076B and is a mixture of talc and mostly chrysotile, according to micro-Raman spectroscopy. The banded veins and talc are commonly crosscut by late orthogonal, extensive lens-shaped veins. They are filled with talc that is locally rimmed by antigorite along the vein walls in talc-rich intervals (e.g. sample 76B-7, Fig. 7c). In contrast, they are filled with serpentine (mainly chrysotile) with frequent carbonates in the center in talc-poor intervals (e.g. sample 76B-8, Fig. 7b).

In the serpentinized peridotites from Hole M0068B, the magnetite-bearing mesh texture occasionally contains olivine relicts between 4 and 4·5 mbsf. Olivine relicts correspond to grains up to 1–2 mm in size, account for only a few per cent of the core's volume, and are generally localized in contact with pyroxenes. Orthopyroxenes in this hole are variably altered to serpentine, talc, tremolite and/or chlorite, whereas tremolite forms from clinopyroxenes locally. Both are also

Table 2: Continued

Sample: Texture:	76B-7 serpentine 2	76B-8 serpentine 2	71B-3 antigorite	71C-5 antigorite	76B-7 antigorite	69A-4 fibrous vein	71C-5 fibrous vein	76B-7 granular vein	76B-8 granular vein	72B-1 mf-related domain	76B-6 mf-related domain	76B-1 mf-related mineral	76B-7 mf-related mineral
SiO_2	43·12	43·98	42·07	43·21	43·79	42·53	43·63	43·95	43·23	39·97	43·82	42·70	44·13
Na_2O	0·03	0·01	0·03	0·02	0·00	0·06	0·00	0·01	0·03	0·02	0·02	0·02	0·03
CaO	0·03	0·04	0·07	0·03	0·02	0·12	0·00	0·04	0·12	0·05	0·04	0·08	0·03
Cl	0·01	0·02	0·02	0·02	0·01	0·17	0·05	0·01	0·03	0·05	0·03	0·03	0·01
FeO	3·81	3·72	5·93	2·29	5·33	3·17	1·86	4·29	6·28	7·41	4·26	7·28	4·79
MgO	38·56	37·17	34·76	39·80	36·43	38·48	39·44	37·92	31·83	34·99	37·02	34·92	36·92
Cr_2O_3	0·00	0·02	0·03	0·01	0·00	0·01	0·00	0·02	0·00	0·02	0·00	0·00	0·00
K_2O	0·02	0·02	0·02	0·01	0·01	0·08	0·01	0·03	0·03	0·00	0·00	0·02	0·00
MnO	0·02	0·02	0·10	0·08	0·07	0·09	0·08	0·09	0·25	0·14	0·05	0·09	0·07
Al_2O_3	0·20	0·16	1·12	0·48	0·01	0·44	0·51	0·18	0·08	0·37	0·33	0·26	0·00
TiO_2	0·03	0·04	0·01	0·02	0·03	0·00	0·03	0·03	0·02	0·06	0·06	0·04	0·01
NiO	0·20	0·19	0·23	0·16	0·09	0·12	0·09	0·03	0·25	0·24	0·31	0·24	0·17
Total	85·99	85·38	84·38	86·15	85·78	85·26	85·69	86·60	82·15	83·32	85·94	85·68	86·17
Si	2·05	2·09	2·05	2·03	2·09	2·03	2·05	2·07	2·16	2·01	2·08	2·07	2·09
Na	0·00	0·00	0·00	0·00	0·00	0·01	0·00	0·00	0·00	0·00	0·00	0·00	0·00
Ca	0·00	0·00	0·00	0·00	0·00	0·01	0·00	0·00	0·01	0·00	0·00	0·00	0·00
Cl	0·00	0·00	0·00	0·00	0·00	0·01	0·00	0·00	0·00	0·00	0·00	0·00	0·00
Fe	0·15	0·15	0·24	0·09	0·21	0·13	0·07	0·17	0·26	0·31	0·17	0·29	0·19
Mg	2·73	2·64	2·53	2·79	2·59	2·74	2·77	2·66	2·37	2·62	2·62	2·52	2·61
Cr	0·00	0·00	0·00	0·00	0·00	0·00	0·00	0·00	0·00	0·00	0·00	0·00	0·00
K	0·00	0·00	0·00	0·00	0·00	0·00	0·00	0·00	0·00	0·00	0·00	0·00	0·00
Mn	0·00	0·00	0·00	0·00	0·00	0·00	0·00	0·00	0·01	0·01	0·00	0·00	0·00
Al	0·01	0·01	0·06	0·03	0·00	0·02	0·03	0·01	0·00	0·02	0·02	0·02	0·00
Ti	0·00	0·00	0·00	0·00	0·00	0·00	0·00	0·00	0·00	0·00	0·00	0·00	0·00
Ni	0·01	0·01	0·01	0·01	0·00	0·00	0·00	0·00	0·01	0·01	0·01	0·01	0·01
OH	4·00	4·00	4·00	4·00	4·00	3·99	4·00	4·00	4·00	4·00	4·00	4·00	4·00
Total	8·95	8·90	8·91	8·95	8·91	8·94	8·93	8·92	8·83	8·97	8·91	8·92	8·91
Total cations	4·95	4·90	4·91	4·95	4·91	4·95	4·93	4·92	4·84	4·98	4·91	4·92	4·91

Additional data are given in Supplementary Data Table S2.

occasionally fresh in the 4–4·5 mbsf interval. The mesh texture and altered pyroxenes are crosscut by lens-shaped serpentine veins that are variably fibrous, granular, isotropic or sometimes composite. Although the material from this hole is not *in situ*, the largest coherent intervals show a preferential orientation of these veins (Fig. 8a). Talc metasomatism is widespread and pervasively affects the cores. It replaces the mesh texture (Figs 6b and 8a, b) but preserves, at least partially, the magnetite concentrations. Talc replacement is total at the contact with metagabbros (grey–green zone at the top of Core M0068B-2R1 in Fig. 3) and progressively decreases away from them, showing a transition to mesh-textured domains (bottom of Core M0068B-2R1).

Hole M0072B is somewhat unique in having the harzburgite crosscut by mafic intrusions; these are surrounded by white domains with light grey haloes propagating into the serpentinized harzburgite (Figs 3 and 7c). At the microscopic scale, pervasive serpentinization has resulted in magnetite-bearing mesh texture with millimeter-sized zones containing olivine relicts that are randomly dispersed in the rock (Figs 5e, 6c and 8d). Local serpentinization degrees are visually estimated to be more than 70%, so that fresh olivine corresponds to only a few per cent of the rock. Magnetite crystallizes in the mesh rims but is poorly concentrated along microfractures (Fig. 5f). The mesh texture is overprinted by a subsequent network of interconnected microfractures (light domains in the thin section in Fig. 8d). The domains that opened along these new microfractures (referred to as microfracture-related domains subsequently) crosscut the pre-existing mesh cells and magnetite concentrations. These domains show sharp edges with no displacement on either side, suggesting that they form as dominantly extensional domains during a brittle event that postdates the onset of serpentinization. They isolate mesh-textured domains that have an average size of 400 μm. The microfracture-related domains are filled by tremolite ± chlorite in the white zones, talc in the light grey haloes, and talc–serpentine mixture to pure serpentine (lizardite and/or chrysotile) a few centimeters away from the white zones. These microfracture-related domains are in contact with dolerite intrusions at the bottom of the hole (Cores M0072B-8R1 and 8R2). They are then crosscut orthogonally by extensive lens-shaped serpentine veins, without preferential orientation at the sample scale. The orthopyroxenes are all altered to serpentine, talc, tremolite and/or chlorite, whereas tremolite forms from clinopyroxenes locally, and some are also moderately deformed. It should be noted that sample 76B-1

Table 3: Representative trace element analyses (in ppm) for primary and serpentine minerals

Sample:	72B-1	76B-6	68B-1	68B-1	68B-1	71C-5	76B-8	71B-3	72B-1	76B-6	71B-3	72B-1	76B-6
Texture:	olivine	olivine	diopside	enstatite	bastite	bastite	bastite	mesh rim	mesh rim	mesh rim	mesh core	mesh core	mesh core
Li	b.d.l.	5·66	5·03	b.d.l.	8·18	1·32	3·47	7·15	b.d.l.	3·48	12·02	b.d.l.	9·58
Sc	4·07	1·66	34·79	32·54	20·10	5·92	20·70	4·36	3·89	1·57	5·47	4·61	1·63
Ti	19·45	19·95	194·88	146·19	72·95	22·55	139·50	25·30	18·42	11·68	27·67	22·29	24·44
V	1·60	0·52	158·13	144·18	99·70	16·55	87·00	11·97	1·84	1·32	13·59	2·23	2·78
Cr	51	6	9230	6115	5100	162	7070	117	61	4	160	93	4
Ni	2925	2780	987	797	1145	1545	1330	1828	2793	2517	2098	2338	2170
Cu	b.d.l.	b.d.l.	6·73	1·25	2·96	2·20	b.d.l.	18·79	b.d.l.	b.d.l.	27·46	b.d.l.	1·89
Zn	32·65	26·35	213·90	43·65	89·05	28·85	20·40	24·30	13·04	12·33	27·84	12·90	16·35
As	0·99	0·86	0·94	1·30	1·90	0·70	0·74	3·46	0·95	0·73	5·55	0·85	0·68
Rb	b.d.l.	b.d.l.	0·51	b.d.l.	0·39	b.d.l.	0·14	0·14	b.d.l.	0·10	0·24	b.d.l.	0·20
Sr	0·13	0·24	4·21	0·13	3·34	1·65	1·21	3·32	0·76	3·70	3·99	0·97	4·56
Y	0·25	0·07	15·69	0·36	4·21	0·30	0·06	0·15	0·26	0·56	0·17	0·34	0·71
Zr	0·11	0·10	2·10	b.d.l.	1·23	b.d.l.	b.d.l.	b.d.l.	0·11	0·04	0·27	0·12	0·16
Nb	0·34	0·02	1·82	0·08	0·26	b.d.l.	0·01	b.d.l.	0·35	b.d.l.	0·01	0·39	b.d.l.
Sn	0·17	0·11	15·66	1·15	0·98	0·13	b.d.l.	0·29	0·13	0·11	0·34	0·20	0·09
Sb	b.d.l.	b.d.l.	0·09	b.d.l.	b.d.l.	b.d.l.	b.d.l.	0·25	b.d.l.	b.d.l.	0·35	b.d.l.	b.d.l.
Cs	b.d.l.	b.d.l.	0·03	b.d.l.	b.d.l.	b.d.l.	b.d.l.	0·05	b.d.l.	b.d.l.	0·07	b.d.l.	b.d.l.
Ba	b.d.l.	b.d.l.	2·11	b.d.l.	0·26	0·26	b.d.l.	0·38	b.d.l.	0·40	0·84	b.d.l.	0·39
La	0·072	0·039	1·819	0·079	0·993	b.d.l.	0·011	0·014	0·102	0·065	0·006	0·134	0·096
Ce	0·166	0·083	9·422	0·203	4·535	0·008	0·033	0·012	0·206	0·241	0·014	0·314	0·285
Pr	0·019	0·010	1·699	0·020	0·766	0·002	b.d.l.	0·002	0·023	0·039	0·004	0·035	0·053
Nd	0·065	0·038	7·696	0·058	3·435	0·010	0·032	b.d.l.	0·107	0·279	0·014	0·126	0·281
Sm	b.d.l.	0·014	2·152	b.d.l.	0·735	b.d.l.	b.d.l.	b.d.l.	0·028	0·101	b.d.l.	0·032	0·093
Eu	0·004	0·007	0·305	0·007	0·149	0·003	0·013	0·014	b.d.l.	0·062	0·011	0·016	0·079
Gd	0·022	b.d.l.	2·354	0·011	0·668	b.d.l.	b.d.l.	b.d.l.	0·026	0·114	b.d.l.	b.d.l.	0·089
Tb	0·003	0·001	0·429	0·002	0·101	0·003	0·001	b.d.l.	0·003	0·013	0·003	0·006	0·014
Dy	0·026	0·010	2·638	0·043	0·597	0·037	0·010	0·017	0·033	0·063	0·015	0·025	0·091
Ho	0·007	0·002	0·556	0·015	0·129	0·009	0·002	0·005	0·007	0·011	0·004	0·007	0·020
Er	0·032	0·012	1·619	0·075	0·415	0·042	0·010	0·013	0·040	0·024	0·016	0·044	0·057
Tm	0·008	0·002	0·207	0·021	0·065	0·007	0·003	0·005	0·009	0·002	0·008	0·013	0·006
Yb	0·104	0·019	1·330	0·144	0·460	0·058	0·008	0·045	0·082	0·016	0·038	0·126	0·052
Lu	0·026	0·003	0·185	0·030	0·085	0·013	0·003	0·010	0·023	0·004	0·011	0·031	0·006
Hf	b.d.l.	b.d.l.	0·178	b.d.l.	0·089	b.d.l.	b.d.l.	b.d.l.	0·007	b.d.l.	b.d.l.	0·006	b.d.l.
Ta	0·012	b.d.l.	0·076	b.d.l.	0·027	b.d.l.	b.d.l.	b.d.l.	0·012	b.d.l.	b.d.l.	0·025	b.d.l.
Pb	b.d.l.	b.d.l.	1·365	0·066	0·070	0·084	b.d.l.	0·390	b.d.l.	b.d.l.	0·444	0·018	b.d.l.
Th	0·029	0·006	0·068	b.d.l.	0·183	b.d.l.	0·004	b.d.l.	0·028	b.d.l.	b.d.l.	0·039	0·017
U	0·018	0·003	0·107	0·038	0·728	1·795	0·215	0·375	0·024	0·001	0·502	0·025	0·135

(continued)

(Core M0076B-2R1) also contains olivine relicts locally and a mesh texture crosscut by local microfracture-related domains predominantly filled by talc. This suggests that the top of Hole M0076B shows similarities to Hole M0072B.

MINERAL CHEMISTRY

Major elements

Primary mineral chemistry (Tables 2 and Supplementary Data S2) is in agreement with compositions previously measured in peridotite samples at the Atlantis Massif (Boschi, 2006). Olivine relicts could be analyzed in four samples (68B-1, 72B-1, 76B-1, 76B-6), their Mg# ranging between 0·87 and 0·91. The rare fresh pyroxenes (three occurrences in sample 68B-1) correspond to orthopyroxene (Mg# 0·91–0·92). They have lower FeO and NiO contents than olivine (Fig. 9; see details in caption) but higher and variable Al_2O_3 (0·4–2·8 wt %) and Cr_2O_3 (0·2–0·7 wt %) contents. Spinels from six samples have Cr# mostly around 0·38–0·45. Major elements in the serpentine minerals are relatively homogeneous, with limited variations between textures, samples, holes or sites. Most of the serpentine phases have a Mg# above 90 and an inferred water or volatile content of around 13–18 wt %. Their NiO and FeO compositions are mostly below that of olivine (Fig. 9), reflecting loss of NiO and FeO to form magnetite. Bastites are the most enriched in Al_2O_3 (up to 6·8 wt %) and Cr_2O_3 (up to 1·1 wt %), mimicking the initial orthopyroxene compositions. The other serpentine textures mostly remain below 0·6 wt % Al_2O_3 and 0·1 wt % Cr_2O_3, despite local enrichments (e.g. Al_2O_3 concentrations between 1 and 2 wt % in 71A-1).

As shown for Hole M0076B, most of the serpentine minerals from the mesh texture are close to the composition of stoichiometric serpentine, whereas antigorite has a slightly higher Si/Mg ratio (Fig. 10; see details in caption). The composition of the transition domains is intermediate between serpentine and talc, suggesting intergrowth of these phases in this texture,

Table 3: continued

Sample:	72B-1	76B-6	68B-1	68B-1	68B-1	71C-5	76B-8	71B-3	72B-1	76B-6	71B-3	72B-1	76B-6
Texture:	serpentine 2	serpentine 2	antigorite	antigorite	antigorite	fibrous vein	banded vein	banded vein	banded vein	mf-related domain	mf-related domain	transition domain	transition domain
Li	16·95	41·25	4·54	b.d.l.	10·70	15·90	9·63	12·50	7·89	10·35	1·79	116·72	62·27
Sc	5·29	4·04	1·76	8·31	1·15	5·26	1·52	0·82	0·80	5·66	1·14	5·48	6·57
Ti	17·45	4·69	14·15	22·40	13·70	25·35	89·05	7·03	3·17	17·75	81·35	14·55	12·61
V	8·71	2·92	5·95	22·20	3·91	12·43	11·65	4·05	1·76	17·75	2·06	2·28	37·07
Cr	35	26	b.d.l.	87	b.d.l.	108	2	3	b.d.l.	446	55	30	103
Ni	2100	5710	422	770	849	1230	994	704	720	1730	1305	5419	7032
Cu	2·41	7·27	b.d.l.	b.d.l.	b.d.l.	15·25	0·71	4·53	b.d.l.	21·70	0·55	b.d.l.	17·63
Zn	19·00	23·60	28·85	32·65	18·75	29·10	24·35	35·40	12·85	35·15	8·62	40·32	30·82
As	2·34	0·96	1·22	0·75	1·57	2·71	1·52	1·25	0·76	3·01	0·65	1·62	9·17
Rb	0·22	0·64	0·99	0·10	0·30	0·31	0·15	0·20	b.d.l.	0·37	0·21	6·08	0·96
Sr	5·03	17·45	0·96	0·67	4·15	3·01	10·04	3·08	1·91	6·25	0·75	36·22	83·21
Y	0·47	0·09	0·44	0·12	0·12	0·15	1·28	0·18	0·05	1·37	0·31	0·08	1·10
Zr	b.d.l.	b.d.l.	b.d.l.	b.d.l.	b.d.l.	0·23	0·39	b.d.l.	b.d.l.	0·33	0·19	b.d.l.	b.d.l.
Nb	b.d.l.	b.d.l.	b.d.l.	b.d.l.	b.d.l.	0·01	0·02	b.d.l.	b.d.l.	0·19	0·10	b.d.l.	b.d.l.
Sn	0·51	0·31	0·47	0·12	0·17	0·21	0·15	0·63	0·13	1·74	0·29	0·15	0·99
Sb	0·09	0·07	b.d.l.	b.d.l.	0·07	0·16	0·15	0·10	b.d.l.	0·13	b.d.l.	b.d.l.	1·26
Cs	b.d.l.	0·09	0·09	b.d.l.	b.d.l.	0·10	b.d.l.	0·02	b.d.l.	0·04	b.d.l.	0·43	0·07
Ba	0·50	0·53	b.d.l.	b.d.l.	0·31	0·65	2·52	1·15	0·14	0·19	b.d.l.	0·96	17·00
La	0·056	0·031	0·239	0·005	0·024	0·005	0·417	0·312	b.d.l.	0·764	0·123	0·031	1·342
Ce	0·151	0·063	0·720	b.d.l.	0·068	0·017	0·904	0·330	0·016	1·665	0·294	0·062	2·691
Pr	0·029	0·008	0·090	b.d.l.	0·007	0·002	0·158	0·026	b.d.l.	0·178	0·032	0·006	0·266
Nd	0·145	0·040	0·344	b.d.l.	0·041	0·023	0·853	0·110	0·021	0·562	0·162	b.d.l.	1·055
Sm	0·047	b.d.l.	0·080	b.d.l.	0·018	b.d.l.	0·221	0·018	b.d.l.	0·121	0·031	b.d.l.	0·179
Eu	0·091	0·047	0·016	b.d.l.	0·030	b.d.l.	0·325	0·027	b.d.l.	0·200	0·048	b.d.l.	2·233
Gd	0·066	b.d.l.	0·076	b.d.l.	0·017	b.d.l.	0·250	0·025	b.d.l.	0·113	0·040	b.d.l.	0·166
Tb	0·012	0·002	0·013	0·002	0·004	0·002	0·037	0·004	0·001	0·022	0·007	b.d.l.	0·019
Dy	0·078	0·012	0·075	0·014	0·025	0·026	0·233	0·027	0·008	0·182	0·039	b.d.l.	0·086
Ho	0·019	b.d.l.	0·012	0·004	0·003	0·006	0·056	0·007	0·004	0·046	0·009	b.d.l.	0·022
Er	0·056	0·008	0·046	0·024	0·010	0·017	0·143	0·019	0·009	0·167	0·039	0·007	0·091
Tm	0·009	b.d.l.	0·009	0·004	0·002	0·004	0·025	0·003	0·002	0·028	0·004	0·002	0·018
Yb	0·083	0·018	0·050	0·031	0·020	0·029	0·147	0·028	0·009	0·270	0·051	0·018	0·148
Lu	0·014	0·005	0·006	0·006	b.d.l.	0·004	0·026	0·006	b.d.l.	0·043	0·010	0·005	0·033
Hf	b.d.l.	b.d.l.	b.d.l.	b.d.l.	b.d.l.	b.d.l.	b.d.l.	b.d.l.	b.d.l.	0·030	b.d.l.	b.d.l.	b.d.l.
Ta	b.d.l.	b.d.l.	b.d.l.	b.d.l.	b.d.l.	b.d.l.	b.d.l.	0·002	b.d.l.	0·014	0·005	b.d.l.	b.d.l.
Pb	0·071	0·309	b.d.l.	b.d.l.	b.d.l.	0·160	0·044	1·147	0·028	0·182	0·015	0·027	4·708
Th	0·001	b.d.l.	b.d.l.	b.d.l.	b.d.l.	b.d.l.	b.d.l.	b.d.l.	b.d.l.	0·177	0·017	b.d.l.	b.d.l.
U	2·620	4·520	b.d.l.	0·158	0·838	0·208	0·825	1·093	0·762	0·173	0·007	0·002	7·247

b.d.l., below detection limit. Additional data are given in Supplementary Data Table S3.

as suspected after micro-Raman spectroscopy. Departure of the serpentine minerals from stoichiometric serpentine remains too small to indicate brucite intergrowths.

Trace elements

The serpentine minerals retain relatively homogeneous trace element concentrations between the successive textures at the sample scale (Table 3). In contrast, rare earth elements (REE) and other elements, including some large ion lithophile elements (LILE), high field strength elements (HFSE) or fluid-mobile elements (FME) clearly exhibit differential enrichments between samples from one site to the other, and even downhole in Hole M0076B.

CI chondrite-normalized REE concentrations of the primary and serpentine minerals are presented in Fig. 11. Most of the REE patterns of serpentine minerals lie between those of olivine and pyroxenes (see details in caption). With some exceptions, serpentine minerals display homogeneous REE patterns in a given sample, which allows classification of the holes into three groups: (1) light REE (LREE)-depleted patterns (Fig. 11a–c) in samples from Site M0071 and probably Site M0069, although the patterns are too incomplete to be presented; (2) U-shaped patterns (Fig. 11g and h) owing to middle REE (MREE) apparent depletion compared with LREE and heavy REE (HREE) in samples from Holes M0068B and M0072B; (3) intermediate, almost flat, patterns (Fig. 11d–f). Three of the four analyzed samples from Hole M0076B exhibit type (3) patterns, with small variations marking the transition between the two previous groups from the bottom (slightly LREE-depleted) to the top (slightly U-shaped). In the fourth sample (Fig. 11i), the REE patterns mimic those of clinopyroxenes that are present in a centimeter-wide vein in the sample (e.g. Tamura *et al.*, 2008; Seyler *et al.*, 2011). Positive Eu anomalies are visible in seven samples and affect most of the textures studied. Only a

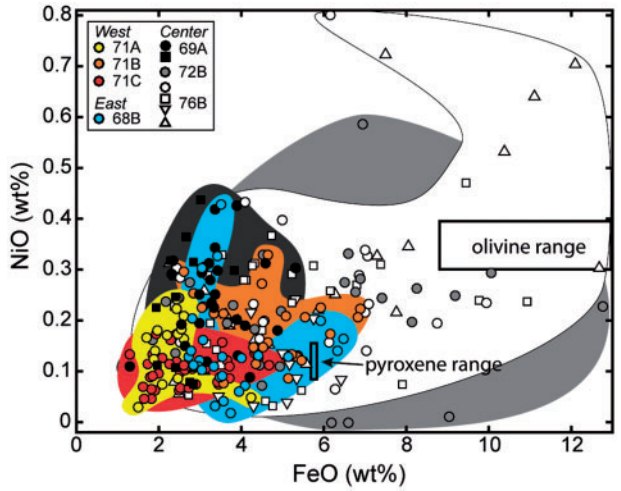

Fig. 9. NiO vs FeO contents acquired with the electron microprobe in primary and serpentine minerals. The colored fields indicate data acquired on samples (symbols) from the same hole, and the black rectangles are the compositional ranges of olivine and pyroxenes. Olivine is richer in both FeO (8·8–13·0 wt %) and NiO (0·3–0·4 wt %) compared with orthopyroxenes (5·73–5·82 wt % and ~0·1 wt %). The NiO contents of the serpentine minerals are the same as or below the concentrations in olivine with a few local exceptions (up to 0·8 wt %). NiO concentrations are higher in the mesh texture than in bastite and decrease in subsequent serpentine textures (serpentine 2, antigorite, and serpentine veins). In all samples, the serpentine minerals have FeO concentrations that are lower than those in olivine, which is consistent with magnetite crystallization during serpentinization. The serpentine iron content ranges between 1 and 12 wt % in Holes M0072B and M0076B and between 1 and 7 wt % in the other holes.

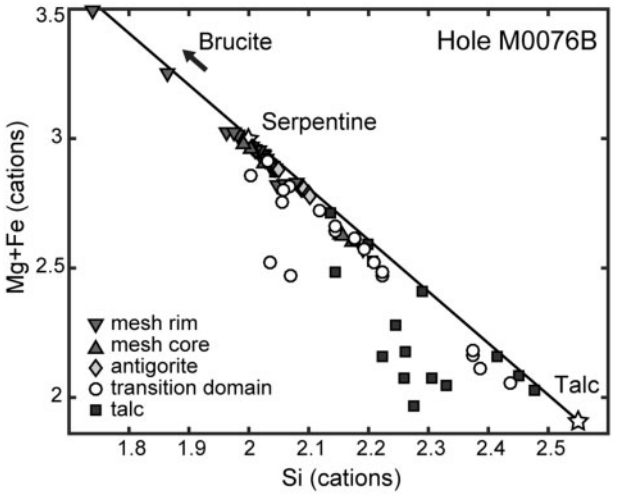

Fig. 10. Number of octahedral (primarily Mg, Fe) vs tetrahedral (Si) cations in serpentine minerals from the mesh rims (lizardite) and mesh cores (lizardite ± chrysotile), and in antigorite, transition domains, and talc in Hole M0076B. The structural formulae are calculated on the basis of seven oxygen atoms. The overall data lie along a trend line joining the stoichiometric Mg–Fe end-member talc (Si = 2·55, Mg + Fe = 1·91), serpentine (Si = 2, Mg + Fe = 3), and brucite (Si = 0, Mg + Fe = 7). Most of the serpentine minerals from the mesh rims and cores plot around the stoichiometric composition of serpentine; a few show deviations of ±0·2 in Si and ±0·5 in Mg + Fe. In comparison, antigorite data are grouped to slightly enriched Si (~2·1) and depleted Mg + Fe values (~2·8), which is also the case for antigorite from the other holes. The analyzed talc is systematically depleted in Si and enriched in Mg + Fe compared with stoichiometric talc, suggesting possible intergrowths with relict serpentine. Depletion in Mg + Fe compared with the trend line is explained by replacement of Mg and Fe by Al in the octahedral sites, these talc zones containing up to 3·84 wt % Al_2O_3, which may also reflect fine-grained chlorite intergrowths. The transition domain minerals follow the trend, despite local depletions in Mg + Fe, with compositions lying between serpentine and talc, suggesting intergrowth of these minerals in this texture as indicated by micro-Raman spectroscopy. It should be noted that the departure of the serpentine minerals from stoichiometric serpentine remains too small to indicate brucite intergrowths. This is also verified in the other analyzed samples.

few recrystallized serpentines, antigorites and veins have flat to negative Eu anomalies in samples 68B-1, 72B-1 and 76B-6 (Fig. 11g–i). Negative Ce anomalies are developed in samples 71A-1 and 71B-3 (Fig. 11a and b), although this does not appear to be systematic and is hard to characterize because of the incomplete patterns.

LREE (e.g. La in Fig. 12) are the least enriched at Sites M0069 and M0071 (~10^{-2} ppm), intermediate in Hole M0076B (10^{-2} to 10^{-1} ppm), and the most enriched in Holes M0068B and M0072B (10^{-1} to 1 ppm). La is plotted versus Nb, Y, Cu, and Sr in Fig. 12, and versus Ta, Th, As, Sb, U, and B in Supplementary Data Fig. S2. Nb, as well as Ta and Th (although Sites M0069 and M0071 are below detection limits for Th), positively correlates with La. Samples from Sites M0069 and M0071 have the lowest Nb values (around 10^{-2} ppm), those from Holes M0068B and M0072B the highest (10^{-1} to 1 ppm), and those from Hole M0076B are intermediate (10^{-2} to 10^{-1} ppm, Fig. 12a). Y displays a comparable trend (Fig. 12b) with values between 10^{-2} and 10 ppm, with the exception of samples from Site M0071 and Hole M0076B, which show local enrichments and depart from the trend. Cu, as well as As and Sb, behaves differently. The highest concentrations are found in serpentine minerals from Holes M0068B, M0069A, and M0071AB (mostly around 10 ppm for Cu), whereas the lowest are in Holes M0071C, M0072B and M0076B (1–2 ppm, Fig. 12c). In the case of Sr (Fig. 12d) and U, Holes M0068B, M0071AB, and M0076B are the most enriched (2–10 ppm for Sr), whereas Holes M0069A, M0072B, and M0071C are less enriched (<1 ppm). Primary mineral relicts were analyzed in samples from Holes M0068B, M0072B, and M0076B. Serpentine minerals have Nb, Ta, and Th concentrations intermediate between the olivine and the pyroxenes in Holes M0072B and M0076B, but are higher in Hole M0068B. The other elements (Y, Cu, As, Sb, U, Sr) are generally enriched in serpentine minerals compared with primary minerals.

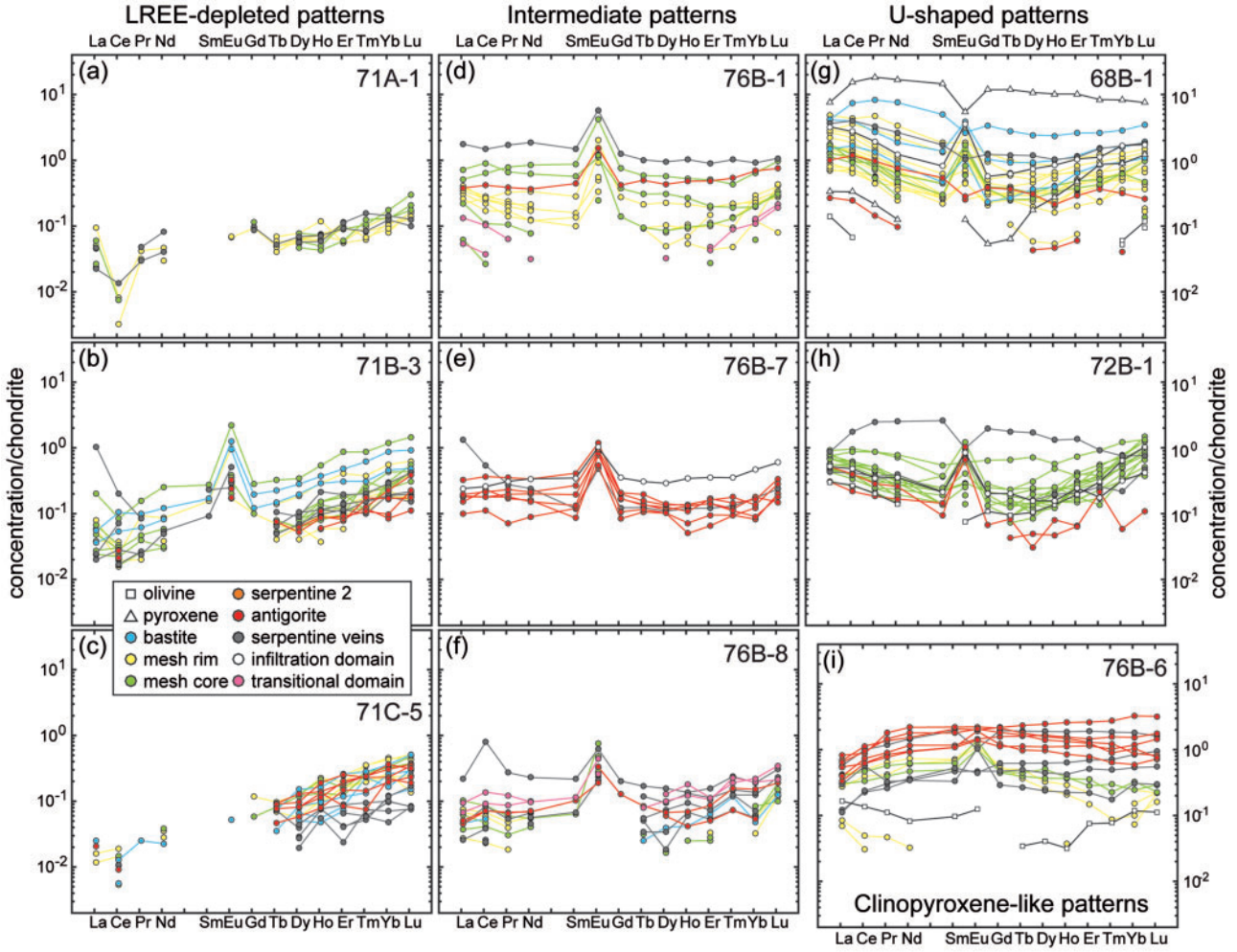

Fig. 11. Chondrite-normalized REE patterns of primary and serpentine minerals in nine of the selected samples. Concentrations below detection limits result in incomplete REE patterns in some cases. Olivine relicts display apparent depletions in MREE compared with LREE and MREE. Whereas the olivine pattern is likely to have a U shape in sample 72B-1, the one in sample 76B-6 appears flatter with a sharp step between Tb and Eu. Olivine patterns in sample 68B-1 are too incomplete to be interpreted, but two pyroxene relicts were found in this sample. An orthopyroxene pattern also displays a U-shaped pattern with a sharp step between Gd and Eu that marks either a positive Eu anomaly or an enrichment similar to the olivine pattern in sample 76B-6. The second pattern corresponds to a clinopyroxene, with a slight linear enrichment from HREE to lighter REE and a depletion in Ce and La, and a negative Eu anomaly. Serpentine mineral patterns mostly lie between those of olivine and pyroxene. They are homogeneous at the sample scale and display three main behaviors. (a–c) LREE-depleted patterns in which concentrations linearly decrease from HREE to LREE. (d–f) Nearly flat patterns in Hole M0076B with a gradient in LREE concentrations from bottom to top: mostly $<10^{-1}$ in sample 76B-8, around (2–3) $\times 10^{-1}$ in sample 76B-7, and above 2×10^{-1} in sample 76B-1. (g, h) U-shaped patterns in which MREE are depleted compared with LREE and HREE. (i) Sample 76B-6 displays unique patterns that are flat in the HREE–MREE range and LREE-depleted. They mimic the typical patterns of clinopyroxene (e.g. Tamura *et al.*, 2008; Seyler *et al.*, 2011) that are present as a centimeter-wide vein in the sample.

DISCUSSION

Altered peridotites were recovered in seven holes drilled across the Atlantis Massif southern wall during IODP Expedition 357. Although the holes are shallow (maximum 16·5 mbsf), the exceptional core recovery preserved the contacts between lithologies and the textural relationships, allowing characterization of variable alteration histories. Lithologies as well as detailed textural, mineralogical, and geochemical observations point to three types of alteration, as follows.

(1) Cores from Sites M0069 and M0071 are dominated by pervasively serpentinized peridotites that bear magnetite-rich mesh texture, with limited antigorite, and bastite after pyroxenes. At Site M0071, the rare gabbroic intervals are altered to chlorite and tremolite, but these do not affect the mineral assemblages in the serpentinized peridotites. The serpentine minerals are characterized by LREE-depleted REE patterns, no enrichments in Nb, Ta, Th, and Y, but enrichments in Cu, As, and Sb. The main difference is the enrichment in U and Sr at Site M0071 and not at Site M0069.

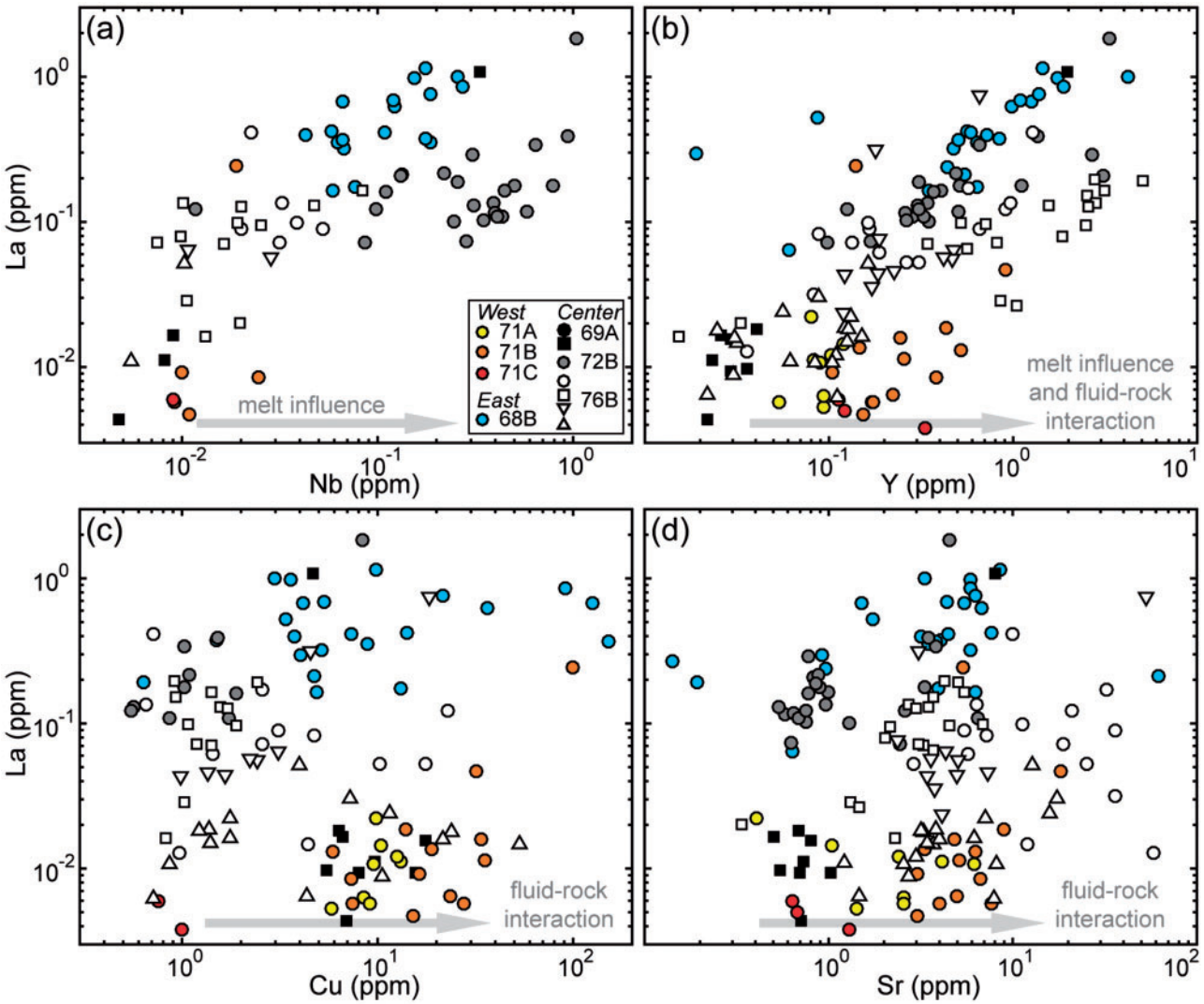

Fig. 12. Examples of trace elements in serpentine minerals showing variable enrichments between the holes. They are plotted versus La and are tracers of melt intrusion (Nb, Y) and fluid–rock (Y, Cu, Sr) interaction in the peridotite. Other elements (Ta, Th, As, Sb, U, B) sharing similar behaviors are plotted in Supplementary Data Fig. S2.

(2) In Holes M0068B and M0072B, the pervasively serpentinized peridotites still contain rare relicts of olivine in samples that are also overprinted by talc-, tremolite- and/or chlorite-dominated intervals associated with mafic intrusions. The serpentine minerals at these two sites have U-shaped REE patterns, with enrichments in Nb, Ta, Th and Y. Hole M0068B is enriched in Cu, As, Sb, U and Sr whereas Hole M0072B is not enriched in these elements.

(3) Hole M0076B shows downhole variations. In the upper half (e.g. samples 76B-1 and 76B-6), pervasively serpentinized peridotites are crosscut by mafic intervals and talc. In the middle part (above 12 mbsf; e.g. samples 76B-7 and 76B-8), they are overprinted by subsequent localized serpentinization leading to serpentine recrystallization and veins, and later talc metasomatism. Serpentine minerals in Hole M0076B show intermediate, flat REE patterns and moderate enrichments in Nb, Ta, Th, and Y. They are enriched in U and Sr, but not in Cu, As, and Sb.

The following discussion investigates what the textures and mineral assemblages reveal about the conditions of serpentinization, and how the geochemical enrichments relate to melt intrusion and fluid–rock interaction. Combining these conclusions, we provide a conceptual model for alteration heterogeneities in the detachment footwall at the Atlantis Massif.

Textural and mineralogical constraints on the heterogeneities of alteration

Background pervasive serpentinization

All the recovered harzburgites and dunites are affected by extensive to full, pervasive serpentinization. This leads to serpentine mesh texture development after olivine, as commonly reported in diverse geodynamic contexts (spreading ridges, ophiolites, subduction

zones, ocean–continent transitions; e.g. Francis, 1956; Wicks & Whittaker, 1977; Prichard, 1979; Viti & Mellini, 1998; Rouméjon & Cannat, 2014). The water is supplied via a network of closely spaced (tens to hundreds of microns) microfractures crosscutting the olivine and delimiting mesh cells. Incipient serpentinization along all the microfracture planes results in pseudo-columnar lizardite growing along these planes and forming the mesh rims (e.g. Viti & Mellini, 1998; Boudier *et al.*, 2010). The pseudo-columns generally do not reach the cell center so that mesh cores are composed of either relict olivine or isotropic serpentine (fine-grained lizardite and/or chrysotile) when serpentinization reaches completion. As suggested by Viti & Mellini (1998), the mesh texture probably results from two successive stages of hydration, reflecting the transition from a closed towards a more open system. The first stage occurs under low water/rock ratios in which all the fluid is consumed by the reaction with olivine; the second occurs under higher water/rock ratios, where the fluid is in excess, favoring the nucleation and growth of many disoriented crystals that lead to isotropic texture in the cores.

In all samples, the mesh rims contain significant amounts of magnetite. Magnetite consumes the iron initially contained in primary minerals that has not been incorporated in serpentine (e.g. Andreani *et al.*, 2013). Its ubiquitous presence underlines the reducing character of serpentinization reactions and suggests significant production of H_2 that ultimately is enriched in the hydrothermal fluids (e.g. Charlou *et al.*, 2002; Proskurowski *et al.*, 2006; Marcaillou *et al.*, 2011). Experiments as well as thermodynamic models have shown that magnetite formation is favored above 200°C and remains limited below (Seyfried *et al.*, 2007; Klein *et al.*, 2009, 2013; Lafay *et al.*, 2012; Malvoisin *et al.*, 2012). Investigations on natural samples confirm that iron is incorporated in magnetite rather than in Fe-rich serpentine and brucite at temperatures higher than 200°C (Klein *et al.*, 2014). We therefore suggest that the onset of the pervasive serpentinization event occurred at temperatures above 200°C at all sites. In addition, temperatures were probably below 350°C, which is the experimentally determined maximum temperature for efficient olivine serpentinization (Martin & Fyfe, 1970; Allen & Seyfried, 2003; Malvoisin *et al.*, 2012). This estimate can further be constrained by re-evaluating oxygen isotope data for magnetite-bearing serpentinites recovered during dives on the southern wall of the Atlantis Massif (Boschi *et al.*, 2008). The above-cited researchers reported temperatures between ~130 and 230°C using the oxygen isotope geothermometer proposed by Früh-Green *et al.* (1996). Applying the most recent calibration for serpentine (Saccocia *et al.*, 2009), we can refine these values to 190–280°C, assuming an isotopic composition of 0‰ for the fluids (Früh-Green *et al.*, 2003) and fluid/rock ratios large enough so that the geothermometer can be applied (Saccocia *et al.*, 2009). Alternatively, more evolved fluids resulting from interaction with both mafic and ultramafic lithologies could have participated in serpentinization. Such fluids could reach an oxygen isotopic composition of 2·4‰ (Campbell *et al.*, 1988), which would imply temperatures between 220 and 350°C. These two extreme cases both agree with a minimum serpentinization temperature around 200°C and a maximum temperature within the efficient serpentinization range.

In general, the pyroxenes in the Atlantis Massif drill cores are equally or more altered compared with olivine. Bastite occurrences are found in almost every harzburgite sample and orthopyroxene replacement by talc, tremolite and/or chlorite also occurs in the central and western sites at Holes M0068B, M0072B, and M0076B. Previous studies have shown that orthopyroxene dissolution is faster than that of olivine at temperatures above 350–400°C (Janecky & Seyfried, 1986; Allen & Seyfried, 2003) favoring talc and tremolite (e.g. Bach *et al.*, 2004). The presence of talc and tremolite after pyroxenes in Holes M0068B, M0072B, and M0076B may therefore indicate that hydration started at temperatures above 350–400°C and that pyroxene alteration predates the onset of serpentinization. These minerals are characteristic of greenschist-facies conditions, indicating temperatures below 500°C. In contrast, only bastite pseudomorphs were found at Site M0071, suggesting that hydration started within the temperature range of serpentinization, of the order of 200–350°C as previously discussed.

Brucite–serpentine intergrowths were observed in mesh textures in serpentinites recovered during ODP Leg 209, mainly in dunites (Bach *et al.*, 2004; 2006), and in olivine-rich troctolites drilled during IODP Legs 304/305 (Beard *et al.*, 2009). In both cases, the composition of these assemblages is intermediate between the serpentine and brucite end-members in octahedral versus tetrahedral cation diagrams (e.g. Beard *et al.*, 2009). In our study, brucite could not be detected visually or by X-ray diffraction on bulk-rock samples (Früh-Green *et al.*, 2017). Additionally, a brucite signature was absent in the micro-Raman spectra, which together with the nearly stoichiometric serpentine compositions of the mesh texture serpentine minerals (e.g. Fig. 10) strongly suggest that brucite is absent in the serpentinized peridotites that make up the southern wall of the Atlantis Massif. This absence can be explained by the presence of moderately to highly Si-enriched hydrothermal fluids (see below) that destabilize brucite into serpentine or prevent its growth, or by significant fluid–rock interaction leading to the dissolution of early formed brucite and its replacement by serpentine and magnetite (Bach *et al.*, 2006; Frost & Beard, 2007).

Continuing and localized serpentinization

The mesh texture is locally overprinted by one or several serpentine recrystallization textures or veins. In particular, cores recovered in Hole M0076B host complex crystallization sequences: centimeter-wide bands of

recrystallized serpentine 2, replacing the mesh texture, are crosscut in their center by antigorite planes and banded veins (Fig. 6a). A similar sequence has been described in serpentinized peridotites dredged along the easternmost Southwest Indian Ridge (SWIR, 62–65°E; Rouméjon *et al.*, 2015) and has been interpreted as the result of localized, continuing serpentinization driven by intense focused fluid flow through the mesh texture.

Recrystallization of the mesh texture into serpentine 2 corresponds to the transition between lizardite and chrysotile via dissolution–recrystallization processes. Such a transition has been recognized in serpentinized peridotites for decades (Boudier, 1971; O'Hanley, 1991; Katayama *et al.*, 2010; Andreani *et al.*, 2013). According to Normand *et al.* (2002), the degree of supersaturation of the fluids relative to serpentine exerts a major control on the prevalence of chrysotile versus lizardite. Lizardite is favored by a low degree of supersaturation, such as at the onset of serpentinization when the dissolved serpentine content in the fluids remains limited and forms the mesh rims. When water supply increases and fluid–rock interaction becomes more extensive, lizardite dissolution can lead to higher degrees of supersaturation, provided crystallization processes are slower. These conditions favor chrysotile and the development of the serpentine 2 texture in domains where fluid–rock interaction is localized. As documented in Rouméjon *et al.* (2015), polygonal serpentine is likely to form owing to lateral growth of chrysotile (Baronnet & Devouard, 1996) under decreasing degrees of supersaturation. This is eventually marked by a textural transition in the SWIR serpentinized peridotites, but not observed at the Atlantis Massif. As no detailed SEM or TEM observations could be realized and micro-Raman spectra are ambiguous, no conclusion can be made about polygonal serpentine growth after the chrysotile-dominated serpentine 2.

Such a recrystallization texture highlights the permeability pathways that preferentially channel hydrothermal fluids in the bulk serpentinizing peridotite. It marks the transition between an early pervasive serpentinization and a further localized serpentinization. Whereas the mesh texture development pervasively affects the bulk peridotite, the late preferential pathways result in circular (Rouméjon *et al.*, 2015; see their fig. 2c) to lens-shaped (Fig. 7) cells surrounding relicts of mesh-textured cores. These cells have geometries that resemble those found at the mesh texture scale, with alteration starting from the rims of a cell and progressing inwards. As visible in Core M0076B-7R1 (Fig. 3), localized serpentinization affects meter-thick intervals through the background mesh-textured serpentinized peridotite. This change in style also corresponds to a jump in permeability pathway spacing: it increases from the sub-millimeter scale in the mesh texture to almost 10-cm scale in the cores. The further development of antigorite and banded veins in the middle of such domains indicates that they maintain a high degree of permeability and keep channeling hydrothermal fluids with exhumation.

Antigorite is present in Hole M0076B as elongated domains between the serpentine 2 and banded veins. It is also observed throughout the mesh texture in the upper part of the hole (e.g. samples 76B-1 and 76B-6) and at Sites M0068 and M0072. At Site M0071, antigorite systematically develops along a few continuous microfractures of the mesh texture after lizardite. Though relatively frequent, it never exceeds a few per cent of the rock. Antigorite in abyssal peridotites has been attributed to serpentinization temperatures higher than those favoring lizardite and chrysotile (Miyashiro *et al.*, 1969; Früh-Green *et al.*, 1996; Dilek *et al.*, 1997; Beard *et al.*, 2009) or to deformation (Prichard, 1979; Ribeiro da Costa *et al.*, 2008). However, a systematic temperature increase during exhumation is not supported by mineralogical (e.g. talc or tremolite instead of serpentine after orthopyroxenes; Bach *et al.*, 2004) or textural (only localized and limited amounts of antigorite in the different holes) evidence. Similarly, such samples are not deformed, so that deformation is not necessary for its formation. The alternative explanation, which we favor here, is that antigorite results from moderate Si-metasomatism (e.g. Coleman, 1971; O'Hanley, 1991; Schwartz *et al.*, 2013). Owing to its wavy crystalline structure, antigorite contains slightly more silica (tetrahedral) atoms compared with magnesium (octahedral) atoms than the other serpentine minerals. Dissolution of the previous lizardite and/or chrysotile associated with a moderate silica input would favor antigorite crystallization along permeability planes. Antigorite development would therefore highlight local Si-enrichment or Mg-depletion in the hydrothermal fluids. This higher Si/Mg ratio in antigorite compared with the other serpentine minerals is confirmed with microprobe analyses of Hole M0076B (Fig. 10). As suggested by Rouméjon *et al.* (2015), pyroxene dissolution releases moderate amounts of silica and could be a source of such enrichments in the fluids. It also explains the absence of antigorite in dunites compared with harzburgites at Site M0071.

Banded veins open in the center of serpentine 2 domains and are filled with chrysotile ± lizardite. Andreani *et al.* (2004) proposed that each band corresponds to a cracking event followed by the introduction of a new supersaturated fluid that crystallizes chrysotile and polygonal serpentine in the void. As for serpentine 2, we cannot conclude on the presence or absence of polygonal serpentine using Raman spectroscopy. These veins develop as en echelon, lens-shaped veins that ultimately join and form continuous veins (Fig. 7a), offering interconnected pathways for hydrothermal fluid circulation. They may result from the stresses generated by serpentinization-induced volume increases in the surrounding peridotite (Andreani *et al.*, 2007). A similar mechanism is proposed for fibrous veins that open in the mesh texture or across pyroxenes and later textures (e.g. antigorite, banded veins, microfracture-

related domains). The banded veins sometimes show a preferential orientation in core intervals, indicating that these veins accommodate the volume increase at various scales at any stage of fluid–rock interaction. Subsequent fracturing produces veins with variable shapes, textures and infills. As no systematic relationships could be found, they probably correspond to local processes and their influence in the permeability network must be limited.

Mafic intrusions

Static replacement of serpentine by talc occurs in Hole M0068B and between 8 and 12 mbsf in Hole M0076B. Talc metasomatism in serpentinized peridotites has been reported in several locations along the MAR, including the Atlantis Massif (Escartín *et al.*, 2003; D'Orazio *et al.*, 2004; Bach *et al.*, 2004; Boschi *et al.*, 2006*b*). It has been associated with significant fluid–rock interaction and theoretically results from either Si-addition to or Mg-removal from the serpentinized peridotite. In Hole M0068B, talc develops in direct contact with altered gabbros and progresses inside the serpentinized harzburgite (Fig. 3). Given that alteration of mafic rocks releases significant amounts of silica compared with ultramafic rocks (Wetzel & Shock, 2000), we interpret this lithological contact as evidence for Si-addition rather than Mg-removal to explain talc development here. This interpretation agrees with the findings of Bach *et al.* (2004) from cores drilled at ODP Leg 209 Site 1268 and the studies of Boschi *et al.* (2006*a*) on samples recovered during dredges and dives at the Atlantis Massif. At the microscopic scale in samples from Hole M0076B, the transition between talc and the mesh texture occurs via a transitional mesh-like texture (shown in Fig. 7c) with an intermediate composition between serpentine and talc (Fig. 10). We propose that it results from the metasomatism of the mesh texture and represents a transitory stage before complete transformation to talc, although the reason it is found only in this hole is unclear and may simply be related to the limited sampling within the shallow holes. Alternatively, talc may undergo transition to the chrysotile-dominated serpentine 2 via antigorite (Fig. 7c), which can be explained in two ways: (1) talc is coeval with antigorite; it could be favored by a chrysotile precursor instead of lizardite, and the talc–antigorite association would represent a local lateral silica gradient; (2) talc grows after pre-existing antigorite as a result of a secondary and more important Si-addition. Unfortunately, our data do not allow us to favor one of the two hypotheses.

In contrast, the microfracture-related domains described in Hole M0072B (Fig. 8d) do not represent replacement of serpentine by talc, but rather direct localized crystallization of talc from a fluid. As visible in the thin section shown in Fig. 8d, the microfracture-related domains are interconnected and incorporate deformed and altered orthopyroxenes and occasional clinopyroxenes of the harzburgite. Their infill shows a mineralogical gradient at the core scale: tremolite ± chlorite dominate in contact with dolerite intrusions, whereas talc dominates throughout the serpentinized harzburgite (Fig. 3). Amphibole–chlorite schists at the Atlantis Massif have been interpreted as replacement of altered mafic intrusions (Boschi *et al.*, 2006*a*). In our study, we never observed relicts or ghosts of plagioclase or clinopyroxene that could attest to an initial mafic origin of the microfracture-related domains. Core observations indicate that they develop around the dolerites rather than replacing them. Based on their sharp edges and the absence of evidence for shearing, we propose that these domains formed after an episode of extensive fracturing in the peridotite, followed by fluid infiltration, mineral precipitation and mass transfer during alteration of the surrounding dolerites. Mass transfer and Si metasomatism is discussed below. The microfracture-related domains therefore represent a permeability network (average spacing of 400 μm) able to channel the hydrothermal fluids until total infilling by hydrous minerals. They are ultimately overprinted by later serpentine veins. Orthopyroxene softening owing to hydration and conversion to talc, tremolite and/or chlorite (e.g. Escartín *et al.*, 2008) favored their preferential deformation during fracturing. An event of dolerite dike emplacement could have influenced such brittle behavior.

The top of Hole M0076B shows comparable, though less interconnected, domains filled with talc that could derive from similar processes. This hole, as well as Hole M0072B, contains a few olivine relicts in the mesh texture. Serpentinization interruption can be due to either a temperature change out of the range most favorable to serpentinization (200–350°C; Martin & Fyfe, 1970; Malvoisin *et al.*, 2012) or a high silica activity leading to the sluggish direct reaction from olivine to talc (Bach *et al.*, 2004). No mineralogical observations support these hypotheses. Alternatively, we propose that serpentinization did not reach completion because the water supply to olivine was reduced. It is likely that the fracturing event leading to the microfracture-related domains created new permeability pathways in the peridotite, hindering continued channeling of fluids through the mesh texture. As a consequence, magnetite grains remained more scattered in the mesh rims compared with samples that underwent more intense fluid–peridotite interaction (e.g. at Sites M0069 and M0071) and that show magnetite grains concentrated as a thin line along the microfractures (Fig. 5f compared with Fig. 5b). The presence of fine-grained magnetite could then explain the wide range of FeO concentrations in some serpentine minerals (Fig. 9), in that dispersed tiny magnetite grains may have been analyzed with the mesh rim serpentines during microprobe measurements. If this fracturing event is linked with dolerite intrusion, these cores are examples of how much the mafic component of the detachment can influence serpentinization of the peridotites during exhumation.

Element mobility and enrichment in serpentine textures

Mineralogical and chemical observations indicate variable enrichments in major and trace elements between holes. They reflect the mobilization of elements during the successive stages of exhumation as a result of early melt emplacement, serpentinization-related fluid–rock interaction, and later fluid–rock interaction.

Consequences of mafic magma intrusion and alteration

The presence of altered gabbros and dolerites correlates with the crystallization of tremolite, chlorite and talc, and enrichments in several trace elements in serpentine minerals. This reflects melt emplacement in the peridotite followed by mass transfer into the surrounding serpentinized peridotites during fluid–rock interaction.

Tremolite ± chlorite and talc in microfracture-related domains of Hole M0072B and talc after serpentine in Holes M0068B and M0076B require a significant addition of Ca, Al, and Si to the serpentinized peridotites. Such elements are preferentially released during alteration of mafic rocks (Boschi *et al.*, 2006*a*), which is supported by the direct association of these minerals with mafic intrusions in the cores (Fig. 3). The mineralogical gradient in newly opened fractures in Hole M0072B suggests *in situ* consumption of Ca and Al to precipitate tremolite and chlorite at the contacts with the dolerite intrusions. The remaining excess of Si provokes talc crystallization a few centimeters farther away into the serpentinized peridotite. Alternatively, in Holes M0068B and M0076B, Al may be immobile forming chlorite blackwall after gabbros, whereas Ca is either immobile to produce Ca-rich intervals or released to the fluids. Si propagates from tens of centimeters in Hole M0068B to the meter scale in Hole M0076B (Fig. 3), away from the altered gabbros, and leads to the pervasive replacement of serpentine by talc. It should be noted that, at Site M0072, tremolite, chlorite and talc develop after the onset of serpentinization and are often crosscut by later serpentine veins. This indicates that the mobility of these elements is transitory and spatially localized in hydrothermal fluids otherwise in equilibrium with serpentine. In Holes M0068B and M0076B talc textures are not postdated by serpentine but sometimes by carbonates, suggesting that the Si activity must remain relatively high until the end of the 'high-temperature' fluid–rock interaction phase. It should be noted that at Site M0071, the gabbroic intervals are altered to chlorite and amphibole and only very rare talc could be found in the serpentinized peridotites. This absence could be explained by the limited amount of gabbro at this site and hence the low amount of silica and other elements (see below) that can be mobilized.

REE addition to serpentinized peridotites occurs during both melt–rock and fluid–rock interaction (Niu, 2004; Paulick *et al.*, 2006). The diversity of REE patterns between samples could therefore be inherited from the protolith signature. However, the higher concentration in serpentine minerals compared with olivine grains (Fig. 11g–i) indicates that hydrothermal processes also significantly contribute to this diversity. LREE are particularly more mobile in fluids compared with MREE and HREE, leading to their preferential enrichment in the hydrothermal fluids that interact with mafic lithologies. Holes dominated by pervasive serpentinization (Holes M0069A, M0071ABC, Fig. 11a–c) show LREE-depleted patterns that mimic those of refractory abyssal peridotites (e.g. Deschamps *et al.*, 2013) and are therefore minimally affected by fluid–rock interaction. In contrast, U-shaped patterns in Holes M0068B and M0072B (Fig. 11g and h) reflect LREE enrichments owing to the proximity with metagabbros or metadolerites. In Hole M0076B, the patterns are intermediate and nearly flat with a slight, gradual LREE depletion from the top to bottom of the hole (Fig. 11d–f). This correlates with the presence of altered gabbros in the top and the dominance of serpentinized peridotites at the bottom (Fig. 2) and confirms LREE mobility at the meter scale (as for silica), with progressive depletion in the fluids with distance from the mafic source. The efficiency of mafic sources in locally (centimeter scale) controlling the REE composition of the surrounding serpentine minerals is well illustrated in sample 76B-6 (Fig. 11i), a highly serpentinized harzburgite crosscut by a slightly altered clinopyroxene vein. The serpentine minerals in the successive serpentine textures display REE patterns mimicking those of clinopyroxenes (e.g. Tamura *et al.*, 2008; Seyler *et al.*, 2011).

Serpentine minerals show variable concentrations in Nb, Ta, Th and Y, which are preferentially mobilized during melt–rock interaction, and to a lesser extent during fluid–rock interaction (Niu, 2004; Paulick *et al.*, 2006). These elements seem to be mobilized locally and exchanged between the former olivine and pyroxenes, as attested by the intermediate concentrations in serpentine minerals in Holes M0072B and M0076B (Fig. 12a). Part of the enrichment could also come, as for LREE, from hydrothermal fluids transporting these elements from mafic intervals to serpentine minerals in Hole M0068B. Only Y is enriched at Site M0071, possibly reflecting a higher mobility in the fluids compared with the other elements (Fig. 12b).

Deep, syn-serpentinization fluid–rock interaction

Serpentinization has weakly affected the major element composition of the peridotites, pointing to nearly isochemical reactions at the sample scale (e.g. Coleman & Keith, 1971). Most of the serpentine minerals have NiO, Al_2O_3, and Cr_2O_3 contents that lie between the olivine and pyroxene compositions, as is commonly observed in serpentinized peridotites (Deschamps *et al.*, 2013). This corresponds to local exchange between serpentine textures of elements preferentially concentrated in the primary minerals. In addition, the Fe contained in the

primary minerals oxidizes and partly crystallizes as magnetite that is remobilized and progressively concentrated along the preferential permeability pathways, either along microfractures in the mesh texture or along the antigorite and banded vein domains in serpentine 2 recrystallization textures.

Copper, As, and Sb are particularly enriched in the serpentine minerals from Holes M0068B, M0069A, and M0071ABC (Fig. 12c). These elements are mobile in fluids and are considered to be derived from the fresh mantle and may be concentrated in sulfides (e.g. Hattori *et al.*, 2005; Kiseeva *et al.*, 2017). Therefore, leaching of these phases by seawater-derived hydrothermal fluids at the onset of serpentinization could favor redistribution among the serpentine textures. Though it is unclear if sulfides concentrate enough of these elements, the enrichments are evidence of relatively deep (Augustin *et al.*, 2012) and potentially intense fluid–rock interaction in some holes.

At all sites, the REE patterns of serpentine minerals show widespread positive Eu anomalies, or on occasion more negative ones (Fig. 11). Eu anomalies in serpentine minerals are not fully understood. They could mimic the positive anomalies naturally present in plagioclase, transferred by fluids having interacted with mafic rocks. In this case, one would expect a correlation with Sr enrichment (Paulick *et al.*, 2006), which is not observed here. Alternatively, Eu mobility is favored by reducing conditions and is enhanced under high temperatures, low pH, and high Cl contents (Bau, 1991; Allen & Seyfried, 2005). Whereas serpentinization reactions produce reducing conditions, olivine serpentinization leads to high pH and alkaline conditions (Palandri & Reed, 2004) that preclude the development of anomalies (Bau, 1991). It is, however, possible that the alteration of mafic rocks and pyroxenes at higher temperatures leads to more acidic conditions favoring Eu mobility and the development of positive anomalies.

Shallow, post-serpentinization fluid–rock interaction

Sr is concentrated in plagioclase (Coogan *et al.*, 2001; Paulick *et al.*, 2006) and more moderately in clinopyroxene (Table 3) or in seawater (Douville *et al.*, 2002). Although Hole M0072B contains a significant amount of altered mafic intervals, the serpentine minerals have the lowest Sr concentrations (Fig. 12d). In contrast, at Site M0071, where the mineralogical and chemical impact of altered gabbros on serpentinized peridotites seems limited, Sr concentrations in the serpentine minerals are higher. The influence of metagabbros on Sr enrichment in serpentine minerals therefore seems limited here. Alternatively, serpentine minerals have been shown to incorporate or trap significant amounts of Sr during serpentinization or late alteration (Snow *et al.*, 1994; Delacour *et al.*, 2008). Similarly, enrichments in U are not correlated with the presence of altered mafic intrusions. Instead, U is more mobile when oxidized so that enrichments would rather occur under open and oxidizing conditions (e.g. at shallow depths or during seafloor weathering; Niu, 2004) than during serpentinization. This suggests that Sr and U enrichment might have occurred during the entire exhumation and continued on the seafloor. These three elements reveal that some portions of the detachment are subjected to intense interaction with fluids whose composition is still highly comparable with seawater. They therefore underline preferential interaction between poorly evolved, seawater-derived hydrothermal fluids and certain domains of the detachment footwall. Sr and U enrichment in serpentine minerals occurs in all the holes except M0069A and M0072B. Hole M0071C is enriched in U but less in Sr, perhaps suggesting that part of the enrichment is decoupled and controlled by local processes and lithologies.

The five sites studied here lie along an east–west spreading-parallel profile across the Atlantis Massif. The western sites therefore correspond to portions of the lithosphere initially emplaced at shallower depths than the eastern sites, which have been exhumed the longest and possibly subjected to seafloor weathering. However, variations in initial position along the detachment fault zone and length of exposure on the seafloor do not seem to have produced major textural or mineralogical differences between the sites. One potential exception is the negative Ce anomalies in REE patterns from Site M0071 samples (Fig. 11a–c), which could result from seafloor weathering compared with the other sites. Negative Ce anomalies have been considered to develop as a result of prolonged interaction between exhumed serpentinized peridotites and naturally Ce-depleted seawater on the seafloor (e.g. Alibo & Nozaki, 1999; Douville *et al.*, 2002); for example, as observed in samples dredged on the flanks of the SWIR (Rouméjon *et al.*, 2015). However, the low LREE concentrations in the Atlantis Massif samples have resulted in incomplete patterns for most of the analyzed samples, thus making interpretations inconclusive.

A conceptual model for alteration heterogeneities on the southern wall of the Atlantis Massif

The alteration textures, mineral assemblages and mineral chemistries recorded in the IODP Expedition 357 drill cores provide constraints on the exhumation and alteration history at varying positions along the detachment footwall that was exhumed and altered to form the southern wall of the Atlantis Massif. Here we propose a conceptual model that focuses on how alteration heterogeneities develop and are controlled by the transition between pervasive and localized serpentinization and by the presence of mafic intrusions, as illustrated in Fig. 13.

The lack of ductile deformation in gabbros at the central dome (IODP Expedition 304/305 Site 1309) suggests that they were emplaced and crystallized in the residual peridotites before significant strain occurred (Karson

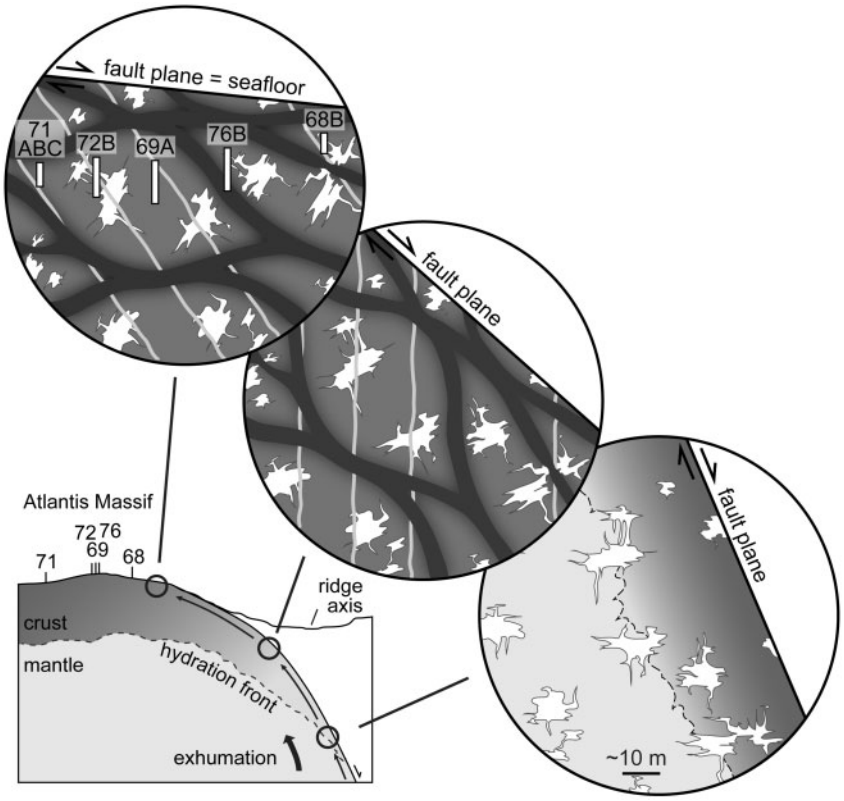

Fig. 13. Conceptual model for the development of alteration heterogeneities in domains of the footwall close to the detachment fault plane at the Atlantis Massif. A flexural rotation of the footwall accompanies the exhumation. Lower circle: fresh peridotites (pale grey), intruded by gabbros (white irregular bodies), are uplifted into the domain of active hydrothermal alteration. There pervasive serpentinization (darker grey) progresses from the fault plane inwards into the footwall. Intermediate circle: as exhumation proceeds, dolerite dikes (light grey lines) crosscut the system and focused fluid flows localize serpentinization along interconnected pathways that hypothetically form cells between a few tens of meters and 100 m in size (dark grey domains). Upper circle: when it reaches the seafloor, this portion of the footwall undergoes weathering and mass wasting. The IODP Expedition 357 drill holes are positioned in this frame, following textural and geochemical arguments (see text).

et al., 2006; Ildefonse *et al.*, 2007). In the recovered cores, harzburgites and dunites correspond to 44% of the total length and gabbroic rocks to 4%. The talc–amphibole–chlorite-bearing rocks represent 11% of the recovered cores and can be interpreted either as serpentinized and metasomatized peridotites (e.g. Fig. 8a and b) or as altered gabbroic intrusions (Boschi *et al.*, 2006*b*). To calculate the initial proportion of gabbros versus peridotite, we take into account and correct for serpentinization-induced volume increase, which can reach 25–45% (e.g. Coleman, 1971). Assuming a volume increase of 30% and assuming that all the talc–amphibole–chlorite-bearing intervals were former peridotites, peridotites would represent 38·5% of the total recovered length. In contrast, if the protolith of the talc–amphibole–chlorite-bearing rocks was gabbroic, peridotites would correspond to 30·8% of the recovered cores. These two end-member volumes correspond to 10–30% gabbros in the peridotites. These estimates are in agreement with those made by Karson *et al.* (2006) that report 70% peridotites and 30% gabbros based on the lithologies of dive samples recovered from the southern wall. However, the distribution and size of the gabbroic bodies remain unconstrained. In the conceptual model shown in Fig. 13, the gabbroic intrusions are drawn with a size of ∼10 m and irregular shapes that finely intrude the surrounding rocks. This size is in agreement with field observations of 'tens of meters' discussed by Karson *et al.* (2006) and reflects the fact that no massive intervals of gabbros were discovered in the IODP Expedition 357 drill holes, with only relatively thin gabbroic intervals (centimeter-thick veinlets to decimeter-thick intervals) present in all the sites, except for a thicker dolerite interval recovered at the top of Hole M0069A. Because of the shallow penetration depths, however, we cannot rule out the possibility that smaller or larger bodies exist but were not drilled.

Alteration commences as the peridotites and gabbros enter the domain of active hydrothermal circulation. Hydration is intense along the detachment fault zone, where the permeability is expected to be the highest (McCaig *et al.*, 2007), and progresses inside the footwall. In some domains, temperatures above 350–400°C favor the replacement of orthopyroxenes by talc or tremolite, whereas olivine is preserved. When the fluids reach temperatures below 350°C, efficient

serpentinization starts and affects the footwall, as recorded by the development of mesh texture at all sites. Based on zircon analyses and multicomponent magnetic remanence data for the central dome, Schoolmeesters *et al.* (2012) proposed a model for the thermal structure of the Atlantis Massif in which the 350°C isotherm would correspond to a depth of ~5 km below the surface. Thus, initiation of serpentinization would have occurred at significant depths and early in the exhumation history of the massif. The infiltration of seawater-derived hydrothermal fluids is facilitated by the closely spaced microfracture network crosscutting the olivine, resulting from combined thermal and tectonic stresses and enhanced by reaction-induced fractures at the onset of serpentinization (Rouméjon & Cannat, 2014). Incipient hydration is likely to provoke dissolution of phases that contain Cu, As, and Sb in the peridotites and Nb, Ta, Th, and Y in the gabbros, and therefore leads to transport and enrichment in the surrounding serpentine minerals. The difference in temperature during initial hydration may indicate different depths of hydrothermal circulation, with some hydrothermal fluids infiltrating the footwall at shallower depths (i.e. slightly lower temperatures) than others. This would imply that fluid supply at the hydration front is locally and temporally heterogeneous (Rouméjon & Cannat, 2014).

As the portion of the footwall reaches shallower levels in the crust, fluid flow is dominated by the most continuous fracture planes, which form permeability pathways and channel the fluids along specific domains of the mesh-textured peridotite. Serpentinization shows a transition from pervasive to localized as indicated by recrystallization of the mesh texture to chrysotile-dominated serpentine 2 and banded veins. Based on the frequent occurrence of similar recrystallization textures in serpentinized peridotites dredged on both sides of the easternmost SWIR, Rouméjon *et al.* (2015) suggested that recrystallized samples were part of broad (1–100 m wide), planar domains, cutting through the background mesh-textured peridotite with a spacing of ~100 m. Core M0076B-7R1 in Hole M0076B (Fig. 3) provides evidence that a continuity exists and that such domains have a planar geometry. Their width is nevertheless limited to ~1 m, at least in this case. We hypothesize that, at larger scales, these planar domains are interconnected in the footwall and form broad cells (intermediate circle in Fig. 13), analogous to the geometries developed in the mesh texture (100–400 μm scale, Rouméjon *et al.*, 2015) and by the recrystallization textures (~10 cm scale). Fluid flow is localized and intense along the edges where the permeability is the highest, but is pervasive and reduced, although still active, within the cells where the permeability is lower.

In Fig. 13, we draw the cells with a preferred orientation subparallel to the detachment fault plane with poorly constrained sizes ranging between a few tens of meters and 100 m. We here propose the hypothesis that if the cells were as small as ~10 m, they would have been sampled in several holes rather than solely in Hole M0076B. The 100 m upper value was suggested by Rouméjon *et al.* (2015), based on the relatively frequent occurrence of recrystallized and veined samples (25% of the samples in 33 dredges) and the typical length of a dredge haul (a few hundred meters) along the easternmost SWIR. If cells were larger than a few hundred meters, a lower proportion of these lithologies would have been recovered. These cells might be comparable with the outcrop patterns described in the Woodsreef serpentinites by O'Hanley & Offler (1992, fig. 3). We also hypothesize that the gabbroic bodies divert fluid flow by acting as relatively impermeable cores. This assumption is based on several arguments: (1) the gabbros do not contain a closely spaced and interconnected fracturing network as developed in the mesh-textured peridotites; (2) pyroxenes as the main mineral constituent in gabbros are more resistant to fracturing than olivine so that the gabbros should be less permeable than the peridotites; (3) no gabbros or mafic intrusions are involved in the interval of localized serpentinization in Hole M0076B, but are instead found above and below. This stage of fluid–rock interaction corresponds to a relatively shallow and open system, in which the compositional signature of seawater in the hydrothermal fluids remains important. It is probably under these conditions that U and Sr enrichment in serpentine minerals initiates. As shown in Hole M0076B, this stage of fluid–rock interaction also corresponds to Si-metasomatism in domains of recrystallized mesh texture, suggesting that fluids carry relatively high concentrations of Si and LREE away from the altered mafic sources.

At least some dolerite dikes crosscut the peridotites and gabbros after the onset of hydration. Two observations help to constrain the timing of intrusion: (1) chilled margins along a dolerite dike in an amphibole–chlorite schist interval from Hole M0075B (Früh-Green *et al.*, 2017) indicate that intrusion occurs after the onset of alteration; (2) in Hole M0072B, microfracture-related domains might result from an event of dolerite intrusion that induced fracturing of the surrounding lithologies. These microfracture-related domains crosscut the partially serpentinized mesh texture so that dolerite intrusion occurs during the pervasive fluid–rock interaction stage. The development of subsequent tremolite–chlorite and talc assemblages indicates that significant amounts of fluids were channeled along these intrusions (Boschi *et al.*, 2006*b*) instead of through the peridotites. In Fig. 13, we draw this stage of dolerite intrusion as vertical pipes, locally overprinted by the large-scale cells.

The upper circle in Fig. 13 represents the final stage in the exhumation history when the portion of the detachment footwall is completely exhumed and subjected to incipient weathering and mass wasting on the seafloor. We have positioned the drilled holes in that frame, although the distances between them are not to scale for clarity purposes. The holes from Sites M0069

and M0071 are characterized by very limited gabbroic contents and dominantly pervasive serpentinization. Therefore, we place these holes away from the main gabbroic bodies and cell edges. The lack of Sr and U enrichments in Hole M0069A suggests that the rocks in this hole weakly interacted with relatively shallow hydrothermal fluids and suggests a position at the center of a cell. Alternatively, the emplacement of a dolerite dike at the top of Hole M0069A may have channeled fluids along its walls instead of through the peridotite. Unfortunately, the present density of sampling does not allow us to test this hypothesis. In contrast, Holes M0071A and M0071B are enriched in Sr and U, which suggests that they were probably in the vicinity of a cell edge. Hole M0071C shows intermediate behavior: enrichments in U as in Holes M0071A and M0071B, but no enrichment in Sr as in Hole M0069A. This hole may be situated a little farther away from the cell edge than the other holes from Site M0071, but still in the vicinity, as these holes were drilled a few hundred meters away from each other. We apply a similar reasoning for Holes M0068B and M0072B. Both are closely linked with gabbroic intrusions, as indicated by the lithologies and LREE concentrations, as well as Nb enrichments in the serpentine minerals. Hole M0068B is enriched in all fluid-mobile elements, whereas Hole M0072B is not. Thus, Hole M0068B was probably situated close to a cell edge whereas M0072B was in the center of a cell. Finally, Hole M0076B is crosscut by a domain of localized serpentinization corresponding to a cell edge and shows moderate Si-metasomatism or LREE-enrichment so that the top was in the vicinity of a gabbroic body.

Similar reasoning could be applied to constrain 100 m to kilometer-sized alteration heterogeneities in detachment systems documented at other locations along the MAR where multiple, closely spaced holes have been drilled; for example, in the Fifteen-Twenty fracture zone (ODP Leg 209; Kelemen *et al.*, 2004) or at the MARK area (23°N, ODP Leg 153; Cannat *et al.*, 1995). It is, however, important to note that the present-day rock recoveries (dredges, drill holes, dives) sample only the shallowest levels of the detachment fault zone, which correspond to domains localized in the vicinity of the fault plane. Therefore, the present model may not apply to domains localized further away inside the footwall.

The proximity of the IODP Expedition 357 drill holes to the fault plane also puts into question how this alteration model links with the detachment-related deformation. Previous work at the Atlantis Massif has shown that the cliffs along the southern wall expose the internal structure of the massif (e.g. Schroeder & John, 2004; Karson *et al.*, 2006). The outcrops reveal that below the sedimentary cover, the massif is composed of an ~100 m thick zone containing strongly foliated to mylonitic serpentinized peridotites and talc–amphibole–chlorite schists. This domain, identified as the detachment shear zone, concentrates an important detachment-related deformation. It overlies a more massive peridotitic-dominant basement, only locally crosscut by mylonitic planes. At the microscopic scale, peridotite samples recovered by dives and dredging record an evolution of the deformation style and distribution with exhumation (Schroeder & John, 2004). Whereas early ductile deformation locally develops as crystal-plastic shear zones in a 500 m thick domain below the fault zone, subsequent semi-brittle deformation is restrained to the 90 m below the inferred fault plane. Semi-brittle deformation was active after the onset of serpentinization and is accommodated by localized tremolite–chlorite schist shear zones. Schroeder & John (2004) concluded that these tremolite–chlorite shear zones weakened the peridotite more than serpentinization itself. They are overprinted by the later brittle deformation in the first 10 m below the fault zone. Our study confirms that serpentinized peridotites themselves are scarcely affected by deformation. Although this could result from the high degree of serpentinization, only rare textures indicate ductile deformation of the primary minerals. Instead, semi-brittle or brittle deformations are mostly accommodated by talc-, amphibole- and/or chlorite-bearing schistose or cataclastic intervals that are derived from mafic lithologies and that crosscut the peridotite (Früh-Green *et al.*, 2017), preserving serpentine textures from deformation.

CONCLUSIONS

We investigated the alteration of peridotites drilled in seven holes at five sites across the southern wall of the Atlantis Massif during IODP Expedition 357. Detailed textural, mineralogical and geochemical investigations reveal variable alteration between holes that represent different portions of the footwall exhumed in the vicinity of the detachment fault plane.

The textural and mineralogical observations indicate that all the harzburgites and dunites underwent a stage of pervasive serpentinization, under temperatures in the range of 200–350°C. This led to a magnetite-bearing mesh texture in which olivine is highly to fully consumed. Alteration of orthopyroxenes to talc, tremolite, or chlorite in Holes M0068B, M0072B, and M0076B suggests that hydration may have started at higher temperatures (400–500°C) in some portions of the footwall. Pervasive serpentinization dominates at the more western Sites M0069 and M0071. In the central Hole M0076B, it is overprinted by further localized recrystallization or vein formation, dominated by chrysotile or antigorite. All these textures record the transition between a pervasive hydration and the emplacement of localized fluid pathways at the initiation of focused and intense fluid–rock interaction. The recrystallization of lizardite into chrysotile or antigorite suggests that both the supersaturation of the fluids relative to serpentine and the Si/Mg ratio of this dissolved material evolve while serpentinization is active. In several holes (Holes M0068B, M0072B, M0076B), alteration of gabbroic or doleritic intrusions leads to tremolite, chlorite and/or talc-bearing textures overprinting the serpentinization textures.

Melt-intrusion as well as syn- and post-serpentinization fluid–rock interaction are recorded by trace element enrichments in serpentine minerals compared with primary minerals. LREE, Nb, Ta, Th and Y enrichments indicate the vicinity of altered mafic intrusions, whereas Cu, As and Sb probably derive from leaching of accessory phases in the mantle at depth. Strontium and U enrichments result from fluid–rock interaction occurring after serpentinization at shallow depths, or during seafloor weathering after complete exhumation.

Our results highlight the specific characteristics of each hole and show that the footwall exhumed at the Atlantis Massif, and probably in any detachment system, is heterogeneous at scales between 100 m and 1 km. The initial mantle peridotite was variably intruded by gabbroic bodies and later dolerite dikes at different lithospheric depths within the footwall. In addition, hydration evolved in time and space, controlled by the evolution of the pathways preferentially used by hydrothermal fluids. Initial pervasive hydration occurs under heterogeneous temperature conditions. As exhumation proceeds, the hydrothermal fluids follow preferential pathways that are interconnected and form large-scale cells. They produce heterogeneous serpentinization assemblages marking intense fluid–rock interaction on cell edges and more limited fluid–rock interaction elsewhere. In parallel, interaction between fluids and mafic intrusions affects the chemistry of the fluids and influences the mineral assemblages and the chemistry of the serpentine minerals in the peridotites with which they later interact.

The presence of the active, highly alkaline hydrothermal system at Lost City indicates that serpentinization processes remain continuing in the southern wall of the Atlantis Massif. The volume of carbonate veins recovered during IODP Expedition 357 was surprisingly low (Früh-Green *et al.*, 2017), even in sites near Lost City, which suggests that present-day fluid flow and hydrothermal activity at Lost City is localized by late normal faults that cut the southern wall (Denny *et al.*, 2015). However, hydrogen and methane anomalies were documented by an extensive water column sampling program and use of a custom sensor package and fluid sampling during IODP Expedition 357. Hydrogen concentrations in bottom waters were elevated above the massif, particularly at sites near Lost City. Methane concentrations were also elevated during drilling, and bubbles were occasionally seen emanating from the seafloor, particularly at Sites M0070 and M0071. These elevated volatile concentrations reflect active serpentinization processes occurring within the sub-seafloor and suggest a flux of hydrogen and methane into bottom seawater at oceanic core complexes.

ACKNOWLEDGEMENTS

We thank the captain and crew of the R.R.S. *James Cook*, the crews of the MeBo and RD2 seabed drills, as well as ECORD and the ESO staff for their efforts and support during all phases of IODP Expedition 357. We also gratefully acknowledge the help provided by Sebastian Cionoiu for the Raman spectroscopy, Lukas Martin for the microprobe, and Marcel Guillong for the LA-ICP-MS. This paper benefited from the constructive reviews of an anonymous reviewer and Wolfgang Bach.

FUNDING

This study was supported by the Swiss National Science Foundation (SNSF) project No. 200021_163187 and SNF contributions to Swiss IODP.

SUPPLEMENTARY DATA

Supplementary data for this paper are available at *Journal of Petrology* online.

REFERENCES

Alibo, D. S. & Nozaki, Y. (1999). Rare earth elements in seawater: particle association, shale-normalization, and Ce oxidation. *Geochimica et Cosmochimica Acta* **63**, 363–372.

Allen, D. E. & Seyfried, W. E. (2003). Compositional controls on vent fluids from ultramafic-hosted hydrothermal systems at mid-ocean ridges: an experimental study at 400°C, 500 bars. *Geochimica et Cosmochimica Acta* **67**, 1531–1542.

Allen, D. E. & Seyfried, W. E. (2005). REE controls in ultramafic hosted MOR hydrothermal systems: an experimental study at elevated temperature and pressure. *Geochimica et Cosmochimica Acta* **69**, 675–683.

Andreani, M., Baronnet, A., Boullier, A.-M. & Gratier, J.-P. (2004). A microstructural study of a "crack-seal" type serpentine vein using SEM and TEM techniques. *European Journal of Mineralogy* **16**, 585–595.

Andreani, M., Mevel, C., Boullier, A.-M. & Escartín, J. (2007). Dynamic control on serpentine crystallization in veins: constraints on hydration processes in oceanic peridotites. *Geochemistry, Geophysics, Geosystems* **8**.

Andreani, M., Muñoz, M., Marcaillou, C. & Delacour, A. (2013). μXANES study of iron redox state in serpentine during oceanic serpentinization. *Lithos* **178**, 70–83.

Augustin, N., Paulick, H., Lackschewitz, K. S., Eisenhauer, A., Garbe-Schönberg, D., Kuhn, T., Botz, R. & Schmidt, M. (2012). Alteration at the ultramafic-hosted Logatchev hydrothermal field: constraints from trace element and Sr–O isotope data. *Geochemistry, Geophysics, Geosystems* **13**.

Bach, W., Garrido, C. J., Paulick, H., Harvey, J. & Rosner, M. (2004). Seawater–peridotite interactions: first insights from ODP Leg 209, MAR 15°N. *Geochemistry, Geophysics, Geosystems* **5**.

Bach, W., Paulick, H., Garrido, C. J., Ildefonse, B., Meurer, W. P. & Humphris, S. E. (2006). Unraveling the sequence of serpentinization reactions: petrography, mineral chemistry, and petrophysics of serpentinites from MAR 15°N (ODP Leg 209, Site 1274). *Geophysical Research Letters* **33**.

Baronnet, A. & Devouard, B. (1996). Topology and crystal growth of natural chrysotile and polygonal serpentine. *Journal of Crystal Growth* **166**, 952–960.

Bau, M. (1991). Rare-earth element mobility during hydrothermal and metamorphic fluid–rock interaction and the significance of the oxidation state of europium. *Chemical Geology* **93**, 219–230.

Beard, J. S., Frost, B. R., Fryer, P., McCaig, A. M., Searle, R. C., Ildefonse, B., Zinin, P. & Sharma, S. K. (2009). Onset and progression of serpentinization and magnetite formation in olivine-rich troctolite from IODP Hole U1309D. *Journal of Petrology* **50**, 387–403.

Blackman, D. K., Cann, J. R., Janssen, B. & Smith, D. K. (1998). Origin of extensional core complexes: evidence from the Mid-Atlantic Ridge at Atlantis Fracture Zone. *Journal of Geophysical Research: Solid Earth* **103**, 21315–21333.

Blackman, D. K., Karson, J. A., Kelley, D. S., Cann, J. R., Früh-Green, G. L., Gee, J. S., Hurst, S. D., John, B. E., Morgan, J., Nooner, S. L., Ross, D. K., Schroeder, T. J. & Williams, E. A. (2002). Geology of the Atlantis Massif (Mid-Atlantic Ridge, 30°N): implications for the evolution of an ultramafic oceanic core complex. *Marine Geophysical Researches* **23**, 443–469.

Blackman, D. K., Ildefonse, B., John, B. E., Ohara, Y., Miller, D. J., MacLeod, C. J. & Expedition 304/305 Scientists. (2006). *Proceedings of the Integrated Ocean Drilling Program, Volume 304/305*. College Station, TX: Integrated Ocean Drilling Program Management International, doi: 10.2204/iodp.proc.304305.2006.

Boschi, C. (2006). Building Lost City: Serpentinization, mass transfer, and fluid flow in an oceanic core complex. PhD thesis (ETH Zürich).

Boschi, C., Früh-Green, G. L., Delacour, A., Karson, J A. & Kelley, D. S. (2006a). Mass transfer and fluid flow during detachment faulting and development of an oceanic core complex, Atlantis Massif (MAR 30°N). *Geochemistry, Geophysics, Geosystems* **7**.

Boschi, C., Früh-green, G. L. & Escartín, J. (2006b). Occurrence and significance of serpentine-hosted talc- and amphibole-rich fault rocks in modern oceanic setting and ophiolite complexes: an overview. *Ofioliti* **31**, 129–140.

Boschi, C., Dini, A., Früh-Green, G. L. & Kelley, D. S. (2008). Isotopic and element exchange during serpentinization and metasomatism at the Atlantis Massif (MAR 30°N): insights from B and Sr isotope data. *Geochimica et Cosmochimica Acta* **72**, 1801–1823.

Boudier, F. (1971). Minéraux serpentineux extraits de péridotites serpentinisées des Alpes Occidentales. *Contributions to Mineralogy and Petrology* **33**, 331–345.

Boudier, F., Baronnet, A. & Mainprice, D. (2010). Serpentine mineral replacements of natural olivine and their seismic implications: oceanic lizardite versus subduction-related antigorite. *Journal of Petrology* **51**, 495–512.

Brazelton, W. J., Schrenk, M. O., Kelley, D. S. & Baross, J. A. (2006). Methane- and sulfur-metabolizing microbial communities dominate the Lost City hydrothermal field ecosystem. *Applied and Environmental Microbiology* **72**, 6257–6270.

Campbell, A. C., Palmer, M. R., Klinkhammer, G. P., Bowers, T. S., Edmond, J. M., Lawrence, J. R., Casey, J. F., Thompson, G., Humphris, S., Rona, P. & Karson, J. A. (1988). Chemistry of hot springs on the Mid-Atlantic Ridge. *Nature* **335**, 514–519.

Cann, J., Blackman, D. K., Smith, D. K., McAllister, E., Janssen, B., Mello, S., Avgerinos, E., Pascoe, A. R. & Escartín, J. (1997). Corrugated slip surfaces formed at ridge–transform intersections on the Mid-Atlantic Ridge. *Nature* **385**, 329–332.

Cannat, M. (1993). Emplacement of mantle rocks in the seafloor at mid-ocean ridges. *Journal of Geophysical Research: Solid Earth* **98**, 4163–4172.

Cannat, M., Karson, J., Miller, D. & Shipboard Scientific 85 Party of ODP Leg 153. (1995). Mid-Atlantic Ridge: Sites 920–924. In: Karson, J. A., Cannat, M., Miller, D. J. & Elthon, D. (eds) *Proceedings of the Ocean Drilling Program, Scientific Results 153*. College Station, TX: Ocean Drilling Program.

Charlou, J.-L., Donval, J.-P., Fouquet, Y., Jean-baptiste, P. & Holm, N. (2002). Geochemistry of high H_2 and CH_4 vent fluids issuing from ultramafic rocks at the Rainbow hydrothermal field (36°14′N, MAR). *Chemical Geology* **191**, 345–359.

Coleman, R. G. (1971). Petrologic and geophysical nature of serpentinites. *Geological Society of America Bulletin* **82**, 897–918.

Coleman, R. G. & Keith, T. E. (1971). A chemical study of serpentinization—Burro Moutain, California. *Journal of Petrology* **12**, 311–328.

Coogan, L. A., Wilson, R. N., Gillis, K. M. & MacLeod, C. J. (2001). Near-solidus evolution of oceanic gabbros: insights from amphibole geochemistry. *Geochimica et Cosmochimica Acta* **65**, 4339–4357.

Delacour, A., Früh-Green, G. L., Frank, M., Gutjahr, M. & Kelley, D. S. (2008). Sr- and Nd-isotope geochemistry of the Atlantis Massif (30°N, MAR): implications for fluid fluxes and lithospheric heterogeneity. *Chemical Geology* **254**, 19–35.

DeMartin, B. J., Sohn, R. A., Canales, J. P. & Humphris, S. E. (2007). Kinematics and geometry of active detachment faulting beneath the Trans-Atlantic Geotraverse (TAG) hydrothermal field on the Mid-Atlantic Ridge. *Geology* **35**, 711.

Denny, A. R., Kelley, D. S. & Früh-Green, G. L. (2015). Geologic evolution of the Lost City hydrothermal field. *Geochemistry, Geophysics, Geosystems* **17**, 375–394.

Deschamps, F., Godard, M., Guillot, S. & Hattori, K. (2013). Geochemistry of subduction zone serpentinites: a review. *Lithos* **178**, 96–127.

Dilek, Y., Coulton, A. & Hurst, S. D. (1997). Serpentinization and hydrothermal veining in peridotites at site 920 in the MARK area. In: Karson, J. A., Cannat, M., Miller, D. J. & Elthon, D. (eds) *Proceedings of the Ocean Drilling Program, Scientific Results 153*. College Station, TX: Ocean Drilling Program, 35–59.

D'Orazio, M., Boschi, C. & Brunelli, D. (2004). Talc-rich hydrothermal rocks from the St. Paul and Conrad fracture zones in the Atlantic Ocean. *European Journal of Mineralogy* **16**, 73–83.

Douville, E., Charlou, J.-L., Oelkers, E. H., Bienvenu, P., Colon, C. F. J., Donval, J.-P., Fouquet, Y., Prieur, D. & Appriou, P. (2002). The Rainbow vent fluids (36°14′N, MAR): the influence of ultramafic rocks and phase separation on trace metal content in Mid-Atlantic Ridge hydrothermal fluids. *Chemical Geology* **184**, 37–48.

Escartín, J., Hirth, G. & Evans, B. (1997). Effects of serpentinization on the lithospheric strength and the style of normal faulting at slow-spreading ridges. *Earth and Planetary Science Letters* **151**, 181–189.

Escartín, J., Mével, C., MacLeod, C. J. & McCaig, A. M. (2003). Constraints on deformation conditions and the origin of oceanic detachments: the Mid-Atlantic Ridge core complex at 15°45′N. *Geochemistry, Geophysics, Geosystems* **4**.

Escartín, J., Smith, D. K., Cann, J. R., Schouten, H., Langmuir, C. H. & Escrig, S. (2008). Central role of detachment faults in accretion of slow-spreading oceanic lithosphere. *Nature* **455**, 790–794.

Falcon-Suarez, I., Bayrakci, G., Minshull, T. A., North, L. J., Best, A. I., Rouméjon, S. & IODP Expedition 357 Science Party. (2017). Elastic and electrical properties and permeability of serpentinites from Atlantis Massif, Mid-Atlantic Ridge. *Geophysical Journal International* **211**, 686–721.

Francis, G. H. (1956). The serpentinite mass in Glen Urquhart, Inverness-Shire, Scotland. *American Journal of Science* **254**, 201–226.

Frost, B. R. & Beard, J. S. (2007). On silica activity and serpentinization. *Journal of Petrology* **48**, 1351–1368.

Früh-Green, G. L., Plas, A. & Lécuyer, C. (1996). Petrologic and stable isotope constraints on hydrothermal alteration and serpentinization of the EPR shallow mantle at Hess Deep (Site 895) 1. In: *Proceedings of the Ocean Drilling Program, Scientific Results, 147*. College Station, TX: Ocean Drilling Program, pp. 255–291.

Früh-Green, G. L., Kelley, D. S., Bernasconi, S. M., Karson, J. A., Ludwig, K. A., Butterfield, D. A., Boschi, C. & Proskurowski, G. (2003). 30,000 years of hydrothermal activity at the Lost City vent field. *Science* **301**, 495–498.

Früh-Green, G. L., Connolly, J. A. D., Plas, A., Kelley, D. S. & Grobety, B. (2004). Serpentinization of oceanic peridotites: implications for geochemical cycles and biological activity the subseafloor biosphere at mid-ocean ridges. In: Wilcock, W. S. D., DeLong, E. F., Kelley, D. S., Baross, J. A. & Craig Cary, S. (eds) *The Subseafloor Biosphere at Mid-Ocean Ridges*. Geophysical Monograph, American Geophysical Union **144**, 119–136.

Früh-Green, G. L., Orcutt, B. N., Green, S. L., et al. (2017). Expedition 357 summary. In: Früh-Green, G. L., Orcutt, B. N., Green, S. L., Cotterill, C. & Expedition 357 Scientists (eds) *Atlantis Massif Serpentinization and Life. Proceedings of the International Ocean Discovery Program, 357*. College Station, TX: International Ocean Discovery Program. doi:10.14379/iodp.proc.357.101.2017

Grimes, C. B., John, B. E., Cheadle, M. J. & Wooden, J. L. (2008). Protracted construction of gabbroic crust at a slow spreading ridge: constraints from $^{206}Pb/^{238}U$ zircon ages from Atlantis Massif and IODP Hole U1309D (30°N, MAR). *Geochemistry, Geophysics, Geosystems* **9**.

Guillong, M., Meier, D. L., Allan, M. M., Heinrich, C. A. & Yardley, B. W. D. (2008). A Matlab-based program for the reduction of laser ablation ICP-MS data of homogeneous materials and inclusions. In: *Mineralogical Association of Canada Short Course Series* **40**, 328–333.

Hattori, K., Takahashi, Y., Guillot, S. & Johanson, B. (2005). Occurrence of arsenic (V) in forearc mantle serpentinites based on X-ray absorption spectroscopy study. *Geochimica et Cosmochimica Acta* **69**, 5585–5596.

Ildefonse, B., Blackman, D. K., John, B. E., Ohara, Y., Miller, D. J. & MacLeod, C. J. (2007). Oceanic core complexes and crustal accretion at slow-speading ridges. *Geology* **35**, 623–626.

Janecky, D. R. & Seyfried, W. E. (1986). Hydrothermal serpentinization of peridotite within the oceanic crust: experimental investigations of mineralogy and major element chemistry. *Geochimica et Cosmochimica Acta* **50**, 1357–1378.

Karson, J. A., Früh-Green, G. L., Kelley, D. S., Williams, E. A., Yoerger, D. R. & Jakuba, M. (2006). Detachment shear zone of the Atlantis Massif core complex, Mid-Atlantic Ridge, 30°N. *Geochemistry, Geophysics, Geosystems* **7**.

Katayama, I., Kurosaki, I. & Hirauchi, K. (2010). Low silica activity for hydrogen generation during serpentinization: an example of natural serpentinites in the Mineoka ophiolite complex, central Japan. *Earth and Planetary Science Letters* **298**, 199–204.

Kelemen, P. B., Kikawa, E., Miller, D. J. & Shipboard Scientific Party of ODP Leg 209. (2004). *Proceedings of the Ocean Drilling Program Initial Reports, 209*. College Station, TX: Ocean Drilling Program.

Kelley, D. S. & Shank, T. M. (2010). Hydrothermal systems: a decade of discovery in slow spreading environments. In: *Geophysical Monograph, American Geophysical Union* **188**, 369–407.

Kelley, D. S., Karson, J. A., Blackman, D. K., Früh-Green, G. L., Butterfield, D. A., Lilley, M. D., Olson, E. J., Schrenk, M. O., Roe, K. K., Lebon, G. T. & Rivizzigno, P. (2001). An off-axis hydrothermal vent field near the Mid-Atlantic Ridge at 30°N. *Nature* **412**, 145–149.

Kelley, D. S., Karson, J. A., Früh-Green, G. L., et al. (2005). A serpentinite-hosted ecosystem: the Lost City hydrothermal field. *Science* **307**, 1428–1434.

Kiseeva, E. S., Fonseca, R. O. C. & Smythe, D. J. (2017). Chalcophile elements and sulfides in the upper mantle. *Elements* **13**, 111–116.

Klein, F., Bach, W., Jöns, N., McCollom, T., Moskowitz, B. & Berquó, T. (2009). Iron partitioning and hydrogen generation during serpentinization of abyssal peridotites from 15°N on the Mid-Atlantic Ridge. *Geochimica et Cosmochimica Acta* **73**, 6868–6893.

Klein, F., Bach, W. & McCollom, T. M. (2013). Compositional controls on hydrogen generation during serpentinization of ultramafic rocks. *Lithos* **178**, 55–69.

Klein, F., Bach, W., Humphris, S. E., Kahl, W.-A., Jöns, N., Moskowitz, B. & Berquo, T. S. (2014). Magnetite in seafloor serpentinite—some like it hot. *Geology* **42**, 135–138.

Konn, C., Charlou, J. L., Donval, J. P., Holm, N. G., Dehairs, F. & Bouillon, S. (2009). Hydrocarbons and oxidized organic compounds in hydrothermal fluids from Rainbow and Lost City ultramafic-hosted vents. *Chemical Geology* **258**, 299–314.

Lafay, R., Montes-Hernandez, G., Janots, E., Chiriac, R., Findling, N. & Toche, F. (2012). Mineral replacement rate of olivine by chrysotile and brucite under high alkaline conditions. *Journal of Crystal Growth* **347**, 62–72.

Lang, S. Q., Butterfield, D. A., Schulte, M., Kelley, D. S. & Lilley, M. D. (2010). Elevated concentrations of formate, acetate and dissolved organic carbon found at the Lost City hydrothermal field. *Geochimica et Cosmochimica Acta* **74**, 941–952.

Lowell, R. P. & Rona, P. A. (2002). Seafloor hydrothermal systems driven by the serpentinization of peridotite. *Geophysical Research Letters* **29**.

Ludwig, K A., Kelley, D. S., Butterfield, D A., Nelson, B. K. & Früh-Green, G. L. (2006). Formation and evolution of carbonate chimneys at the Lost City hydrothermal field. *Geochimica et Cosmochimica Acta* **70**, 3625–3645.

Malvoisin, B., Brunet, F., Carlut, J., Rouméjon, S. & Cannat, M. (2012). Serpentinization of oceanic peridotites: 2. Kinetics and processes of San Carlos olivine hydrothermal alteration. *Journal of Geophysical Research: Solid Earth* **117**.

Marcaillou, C., Muñoz, M., Vidal, O., Parra, T. & Harfouche, M. (2011). Mineralogical evidence for H_2 degassing during serpentinization at 300°C/300 bar. *Earth and Planetary Science Letters* **303**, 281–290.

Martin, B. & Fyfe, W. S. (1970). Some experimental and theoretical observations on the kinetics of hydration reactions with particular reference to serpentinization. *Chemical Geology* **6**, 185–202.

McCaig, A. M., Cliff, R A., Escartín, J., Fallick, A. E. & MacLeod, C. J. (2007). Oceanic detachment faults focus very large volumes of black smoker fluids. *Geology* **35**, 935–938.

Michael, P. J., Langmuir, C. H., Dick, H. J. B., Snow, J. E., Goldstein, S. L., Graham, D. W., Lehnert, K., Kurras, G., Jokat, W., Mühe, R. & Edmonds, H. N. (2003). Magmatic and amagmatic seafloor generation at the ultraslow-spreading Gakkel Ridge, Arctic Ocean. *Nature* **423**, 956–961.

Miller, D. J. & Christensen, N. I. (1997). Seismic velocities of lower crustal and upper mantle rocks form the slow-spreading Mid-Atlantic Ridge, South of the Kane transform zone (MARK). In: Karson, J. A., Cannat, M., Miller, D. J. & Elthon, D. (eds) *Proceedings of the Ocean Drilling Program, Scientific Results 153*. College Station, TX: Ocean Drilling Program, pp. 437–454.

Miyashiro, A., Shido, F. & Ewing, M. (1969). Composition and origin of serpentinites from the Mid-Atlantic Ridge near 24° and 30° North Latitude. *Contributions to Mineralogy and Petrology* **23**, 117–127.

Morris, A., Gee, J. S., Pressling, N., John, B. E., MacLeod, C. J., Grimes, C. B. & Searle, R. C. (2009). Footwall rotation in an oceanic core complex quantified using reoriented Integrated Ocean Drilling Program core samples. *Earth and Planetary Science Letters* **287**, 217–228.

Niu, Y. (2004). Bulk-rock major and trace element compositions of abyssal peridotites: implications for mantle melting, melt extraction and post-melting processes beneath mid-ocean ridges. *Journal of Petrology* **45**, 2423–2458.

Normand, C., Williams-Jones, A. E., Martin, R. F. & Vali, H. (2002). Hydrothermal alteration of olivine in a flow-through autoclave: nucleation and growth of serpentine phases. *American Mineralogist* **87**, 1699–1709.

O'Hanley, D. S. (1991). Fault-related phenomena associated with hydration and serpentine recrystallization during serpentinization. *Canadian Mineralogist* **29**, 21–35.

O'Hanley, D. S. & Offler, R. (1992). Characterization of multiple serpentinization, Woodsreef, New South Wales. *Canadian Mineralogist* **30**, 1113–1126.

Oufi, O., Cannat, M. & Horen, H. (2002). Magnetic properties of variably serpentinized abyssal peridotites. *Journal of Geophysical Research* **107**.

Palandri, J. L. & Reed, M. H. (2004). Geochemical models of metasomatism in ultramafic systems: serpentinization, rodingitization, and sea floor carbonate chimney precipitation. *Geochimica et Cosmochimica Acta* **68**, 1115–1133.

Paulick, H., Bach, W., Godard, M., De Hoog, J. C. M., Suhr, G. & Harvey, J. (2006). Geochemistry of abyssal peridotites (Mid-Atlantic Ridge, 15°20′N, ODP Leg 209): implications for fluid/rock interaction in slow spreading environments. *Chemical Geology* **234**, 179–210.

Prichard, H. M. (1979). A petrographic study of the process of serpentinisation in ophiolites and the ocean crust. *Contributions to Mineralogy and Petrology* **68**, 231–241.

Proskurowski, G., Lilley, M. D., Kelley, D. S. & Olson, E. J. (2006). Low temperature volatile production at the Lost City hydrothermal field, evidence from a hydrogen stable isotope geothermometer. *Chemical Geology* **229**, 331–343.

Proskurowski, G., Lilley, M. D., Seewald, J. S., Früh-Green, G. L., Olson, E. J., Lupton, J. E., Sylva, S. P. & Kelley, D. S. (2008). Abiogenic hydrocarbon production at Lost City hydrothermal field. *Science* **319**, 604–608.

Ribeiro da Costa, I., Barriga, F. J. A. S., Viti, C., Mellini, M. & Wicks, F. J. (2008). Antigorite in deformed serpentinites from the Mid-Atlantic Ridge. *European Journal of Mineralogy* **20**, 563–572.

Rouméjon, S. & Cannat, M. (2014). Serpentinization of mantle-derived peridotites at mid-ocean ridges: mesh texture development in the context of tectonic exhumation. *Geochemistry, Geophysics, Geosystems* **15**, 2354–2379.

Rouméjon, S., Cannat, M., Agrinier, P., Godard, M. & Andreani, M. (2015). Serpentinization and fluid pathways in tectonically exhumed peridotites from the Southwest Indian Ridge (62–65°E). *Journal of Petrology* **56**, 703–734.

Saccocia, P. J., Seewald, J. S. & Shanks, W. C. (2009). Oxygen and hydrogen isotope fractionation in serpentine–water and talc–water systems from 250 to 450°C, 50 MPa. *Geochimica et Cosmochimica Acta* **73**, 6789–6804.

Sauter, D., Cannat, M., Rouméjon, S., Andreani, M., Birot, D., Bronner, A., Brunelli, D., Carlut, J., Delacour, A., Guyader, V., MacLeod, C. J., Manatschal, G., Mendel, V., Ménez, B., Pasini, V., Ruellan, E. & Searle, R. (2013). Continuous exhumation of mantle-derived rocks at the Southwest Indian Ridge for 11 million years. *Nature Geoscience* **6**, 314–320.

Schoolmeesters, N., Cheadle, M. J., John, B. E., Reiners, P. W., Gee, J. & Grimes, C. B. (2012). The cooling history and the depth of detachment faulting at the Atlantis Massif oceanic core complex. *Geochemistry, Geophysics, Geosystems* **13**.

Schroeder, T. & John, B. E. (2004). Strain localization on an oceanic detachment fault system, Atlantis Massif, 30°N, Mid-Atlantic Ridge. *Geochemistry, Geophysics, Geosystems* **5**.

Schwartz, S., Guillot, S., Reynard, B., Lafay, R., Debret, B., Nicollet, C., Lanari, P. & Auzende, A. L. (2013). Pressure–temperature estimates of the lizardite/antigorite transition in high pressure serpentinites. *Lithos* **178**, 197–210.

Seyfried, W. E., Foustoukos, D. I. & Fu, Q. (2007). Redox evolution and mass transfer during serpentinization: an experimental and theoretical study at 200°C, 500 bar with implications for ultramafic-hosted hydrothermal systems at mid-ocean ridges. *Geochimica et Cosmochimica Acta* **71**, 3872–3886.

Seyler, M., Brunelli, D., Toplis, M. J. & Mével, C. (2011). Multiscale chemical heterogeneities beneath the eastern Southwest Indian Ridge (52°E-68°E): trace element compositions of along-axis dredged peridotites. *Geochemistry, Geophysics, Geosystems* **12**.

Snow, J. E., Hart, S. R. & Dick, H. J. B. (1994). Nd and Sr isotope evidence linking mid-ocean-ridge basalts and abyssal peridotites. *Nature* **371**, 57–60.

Tamura, A., Arai, S., Ishimaru, S. & Andal, E. S. (2008). Petrology and geochemistry of peridotites from IODP Site U1309 at Atlantis Massif, MAR 30°N: micro- and macro-scale melt penetrations into peridotites. *Contributions to Mineralogy and Petrology* **155**, 491–509.

Viti, C. & Mellini, M. (1998). Mesh textures and bastites in the Elba retrograde serpentinites. *European Journal of Mineralogy* **10**, 1341–1359.

Wetzel, L. R. & Shock, E. L. (2000). Distinguishing ultramafic-from basalt-hosted submarine hydrothermal systems by comparing calculated vent fluid compositions. *Journal of Geophysical Research: Solid Earth* **105**, 8319–8340.

Wicks, F. J. & Whittaker, E. J. W. (1977). Serpentine textures and serpentinization. *Canadian Mineralogist* **15**, 459–488.